TECHNISCHE
UNIVERSITÄT
WIEN

Development and validation of a finite-element model for predicting railway vehicle underfloor noise

Diplomarbeit

Likun LUO

TECHNISCHE
UNIVERSITÄT
WIEN

DIPLOMARBEIT

Development and validation of a finite-element model for predicting railway vehicle underfloor noise

ausgeführt zum Zwecke der Erlangung
des akademischen Grades eines Diplom-Ingenieurs
unter der Leitung von

Assistant Prof. Dipl.-Ing. Dr.techn. Florian Toth
Institut für Mechanik und Mechatronik, E325-03

und

Dipl.-Ing. Michael Steinhauser
Siemens Mobility Austria GmbH
Leberstraße 34, A-1110 Wien

eingereicht an der Technischen Univeristät Wien
Fakultät für Maschinenwesen und Betriebswissenschaften
von

Likun LUO
Matrikelnummer 11771106
Wien, am 20. Jänner 2023

Unterschrift

Affidavit

I declare in lieu of oath, that I wrote this thesis and performed the associated research myself, using only literature cited in this volume. If text passages from sources are used literally, they are marked as such.

I confirm that this work is original and has not been submitted elsewhere for any examination, nor is it currently under consideration for a thesis elsewhere.

I acknowledge that the submitted work will be checked electronically-technically using suitable and state-of-the-art means (plagiarism detection software). On the one hand, this ensures that the submitted work was prepared according to the high-quality standards within the applicable rules to ensure good scientific practice "Code of Conduct" at the TU Wien. On the other hand, a comparison with other student theses avoids violations of my personal copyright.

City and Date

Signature

Abstract

Noise reduction is important in developing a sustainable and environmentally friendly modern rail vehicle. A significant part of the train noise comes from the vehicle underfloor area due to the rolling noise generated at the wheel-rail interface, which could negatively affect the vehicle exterior as well as the interior noise level through different propagation mechanisms. For this reason, it is important to have a meaningful acoustic model that can investigate the underfloor noise already in the initial phase of the vehicle development process.

This thesis presents the development of a 3D finite element model for predicting underfloor noise propagation of rail vehicles. The modeling approach is applied to a one-fourth model of the metro train type X-Wagen from Siemens. The developed model is then validated with an outer pressure field measurement in the car body surroundings. The obtained simulation results show good agreement between the predicted and the measured values. Beyond that, the effect of the variation of certain model parameters on the prediction accuracy of the finite element model is also investigated in the framework of this thesis.

Kurzfassung

Lärmreduzierung ist ein wichtiges Thema bei der Entwicklung eines modernen, nachhaltigen und umweltfreundlichen Schienenfahrzeugs. Ein erheblicher Teil des Zuglärms stammt aus dem Unterflurbereich des Schienenfahrzeugs aufgrund des Rollgeräuschs, das durch den Rad-Schiene-Kontakt erzeugt wird und durch verschiedene Ausbreitungsmechanismen sowohl den Außen- als auch den Innengeräuschpegel des Fahrzeugs negativ beeinflussen kann. Aus diesem Grund ist es von großer Bedeutung, über ein aussagekräftiges Akustikmodell zu verfügen, mit dem das Unterbodengeräusch bereits in der Anfangsphase des Fahrzeugentwicklungsprozesses untersucht werden kann.

In dieser Arbeit wird ein 3D Finite-Elemente-Modell zur Vorhersage der Unterflurlärmausbreitung von Schienenfahrzeugen entwickelt. Der Modellierungsansatz wird auf ein Ein-Viertel-Modell des U-Bahn-Zugs Typ X-Wagen von Siemens angewendet. Das entwickelte Modell wird anschließend mit einer Außendruckfeldmessung in der Wagenkastenumgebung validiert. Die erzielten Simulationsergebnisse zeigen eine gute Übereinstimmung zwischen den vorhergesagten und den gemessenen Werten. Darüber hinaus wird im Rahmen dieser Arbeit auch der Einfluss der Variation bestimmter Modellparameter auf die Aussagekraft des Finite-Elemente-Modells untersucht.

List of Figures

List of Tables

Contents

Chapter 1

Introduction

1.1 Motivation

Modern rail vehicles like trains, metro vehicles or trams have to meet ever increasing acoustic requirements and strict noise legislation not only to improve the acoustic comfort of the passengers, but also to reduce environmental noise pollution caused by the railway transportation [1,7,8]. A significant part of the train noise comes from the vehicle underfloor area, where the bogies and auxiliary equipment, for example, the air supply system, the hydraulic system, or the electric system, are located. The major source of the underfloor noise is the rolling noise emitted by the wheel-rail interface at the bogie area [9]. In addition, for a driven bogie, the operational noise of traction motors also contributes greatly to the overall underfloor noise level [1,10]. The bogie area noise can be transmitted into the car interior through both structure-borne and airborne pathways as depicted in Fig. 1.1. The structure-borne component of the bogie area noise is mainly due to the vibrations of the wheel that are transmitted through the car suspension into the vehicle interior. The airborne component propagates directly into the exterior of the vehicle, disturbing the people in the surroundings and could also be transmitted into the car interior, for example through windows and doors, affecting the comfort of the passenger. Hence, having a computational model that can assess the underfloor noise in the early development phase of the rail vehicle is greatly important and can help in controlling both car exterior and interior noises.

1.2 Aims and objectives

This thesis, conducted in collaboration with Siemens Mobility Austria GmbH, focuses on the propagation of the underfloor noise into the railway vehicle's surroundings and aims to develop a computational model that can predict the pressure field distribution around the vehicle car body due to the bogie area noise, based on the finite element method (FEM). The modeling approach should be applied to the metro train type X-Wagen from Siemens, and an artificial noise source beneath the underframe should be used as excitation. Furthermore, the finite element model is to be validated by an outer pressure field measurement with the vehicle at standstill, which is also a part of this thesis. The developed finite element model in the framework of this thesis should provide a good starting point for the further modeling using the finite element method for the underfloor noise prediction and should accomplish the following main tasks:

- Develop a simulation workflow of the underfloor noise prediction using FEM.
- Assess the applicability of the modeling approach using FEM and determine its limitations.

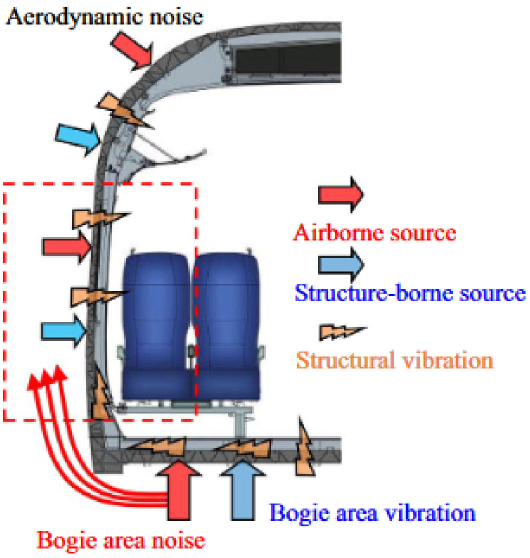

Figure 1.1: Transmission path of exterior noise sources. Figure taken from [1].

It should further answer the following research questions:

- What are the necessary boundary conditions and how can they be incorporated into the finite element model?
- How much of the vehicle and its surroundings can be considered in the model with currently available computational resources?
- How accurate is the prediction of the model and how sensitive are the simulation results with respect to several parameter variations?

1.3 Structure of the thesis

The remainder of this thesis is organized as follows. First, Chapter 2 provides a fundamental background of the thesis. In the chapter, the governing equations and the finite element formulation of the linear acoustic problem are explained, the perfectly matched layer (PML) technique to simulate acoustic open domain is introduced, and important terminologies from the noise measurement technique are summarized. Further, this chapter also gives a brief overview of the metro train type X-Wagen to which the finite element modeling approach will be applied. In Chapter 3, the sound power measurement of the omnidirectional noise source serving as the input for the finite element simulation is carried out. Further, the outer pressure field distribution in the vehicle surroundings due to an artificial noise source beneath the car floor is measured and will be later used as validation for the finite element model. Chapter 4 describes the design and development of the finite element model. A parameter study is carried out to find an optimal simulation domain size of the acoustic open region. The modeling approach of the sound source is introduced to incorporate the measured input sound power into the finite element model. Additionally, besides the initial simulation setup for the underfloor noise prediction, several parameter studies on different model parameters are also prepared to investigate the solution sensitivity. In Chapter 5, the obtained simulation results are compared with the validation measurement to validate the finite element model. Subsequently, the obtained results from the parameter studies are also presented. Finally, Chapter 6 summarizes the thesis and provides an outlook on possible adaptions and extensions to the performed simulations and lists the future work.

Chapter 2

Fundamentals

2.1 Governing equations and finite element formulation

In this section, the governing equations for acoustics and the corresponding finite element formulation are explained following Kaltenbacher [11, 12], Bergman [13] and Heutschi [14].

Linear acoustic wave equation

Assuming an isentropic case, the basic equations of acoustics are based on the conservation of mass

$$\frac{\partial \rho}{\partial t} + \nabla \cdot (\rho \boldsymbol{u}) = 0, \tag{2.1}$$

which is also called the continuity equation and the conservation of momentum

$$\rho \frac{\partial \boldsymbol{u}}{\partial t} + \rho \boldsymbol{u} \cdot \nabla \boldsymbol{u} = -\nabla p + \nabla \cdot [\tau] + \boldsymbol{f}. \tag{2.2}$$

Here, ρ denotes the fluid density, p the fluid pressure, $\boldsymbol{u}$ the particle velocity, $[\tau]$ the viscous stress tensor and $\boldsymbol{f}$ an external force density. If air is used as the medium for sound propagation, it can be considered as an inviscid fluid due to its low viscosity. Hence, $\nabla \cdot [\tau]$ in Eq. (2.2) can be neglected. Moreover, the external force density $\boldsymbol{f}$ will also be neglected.

For linear acoustic wave propagation, the perturbation approach for the three acoustic quantities ρ, p and $\boldsymbol{u}$ is used

$$\rho = \rho_0 + \rho_a; \qquad p = p_0 + p_a; \qquad \boldsymbol{u} = \boldsymbol{u_0} + \boldsymbol{u_a}, \tag{2.3}$$

whereby the quantities are split up in their mean $\square_0$ and alternating part $\square_a$. It is also assumed that the perturbations are small compared to the mean parts

$$\rho_a \ll \rho_0; \qquad p_a \ll p_0; \qquad \boldsymbol{u_a} \ll \boldsymbol{u_0}. \tag{2.4}$$

Furthermore, it is assumed that the mean pressure p_0 and the mean density ρ_0 do not vary over space and time and a quiescent medium with no background flow ($\boldsymbol{u_0} = \boldsymbol{0}$) is considered. Applying the perturbation approach and all assumptions above to the conservation equations Eq. (2.1), Eq. (2.2) and ignoring all second-order terms of the perturbations yields

$$\frac{\partial \rho_a}{\partial t} + \rho_0 \nabla \cdot \boldsymbol{u_a} = 0, \tag{2.5}$$

$$\rho_0 \frac{\partial \boldsymbol{u_a}}{\partial t} + \nabla p_a = \mathbf{0}, \tag{2.6}$$

which are the linearized conservation equations of mass and momentum. Next, by applying a time derivative to Eq. (2.5), a space derivative (divergence) to Eq. (2.6), combining both equations and using the linearized pressure-density relation

$$\rho_a = \frac{p_a}{c_0^2}, \tag{2.7}$$

the linear acoustic wave equation for a homogeneous medium is obtained

$$\frac{1}{c_0^2}\frac{\partial^2 p_a}{\partial t^2} - \nabla \cdot \nabla p_a = 0, \tag{2.8}$$

where c_0 denotes the speed of sound in the propagation medium and depends on the material properties, namely the bulk modulus K_0 and the density ρ_0. Thereby, following relation holds [15, 16]

$$c_0 = \sqrt{\frac{K_0}{\rho_0}}. \tag{2.9}$$

For a sinusoidal wave, which is, for example, excited by a harmonic source, the solution of Eq. (2.8) can be represented as

$$p_a(\boldsymbol{x}, t) = Re\{\hat{p}_a(\boldsymbol{x}) e^{j\omega t}\}, \tag{2.10}$$

with $\hat{p}_a$ being the pressure amplitude and ω being the angular frequency of oscillation. With the restriction to sinusoidal time dependency, the acoustic wave equation can be simplified to

$$\nabla \cdot \nabla \hat{p}_a + \frac{\omega^2}{c_0^2}\hat{p}_a = 0, \tag{2.11}$$

which is the famous Helmholtz equation. The pressure amplitude $\hat{p}_a$ depends only on the position in space.

Finite element formulation

After the abbreviation of the linear acoustic wave equation Eq. (2.8), the weak form (or variational formulation) of the problem is obtained by multiplying the PDE with an appropriate test function p' and integrating over the whole computational domain Ω. Thus, one obtains

$$\text{Find } p_a \text{, such that } \int_\Omega p' \frac{1}{c_0^2}\frac{\partial^2 p_a}{\partial t^2} \mathrm{d}\Omega - \int_\Omega p' \nabla \cdot \nabla p_a \mathrm{d}\Omega = 0 \; \forall p' \,. \tag{2.12}$$

Using the product rule for the divergence

$$\nabla \cdot (f\boldsymbol{g}) = f \nabla \cdot \boldsymbol{g} + \nabla f \cdot \boldsymbol{g}, \tag{2.13}$$

the second term in Eq. (2.12) can be expressed as

$$\int_\Omega p' \nabla \cdot \nabla p_a \mathrm{d}\Omega = -\int_\Omega \nabla p' \cdot \nabla p_a \mathrm{d}\Omega + \int_\Omega \nabla \cdot (p' \nabla p_a) \mathrm{d}\Omega. \tag{2.14}$$

Applying the divergence theorem [17,18]

$$\int_\Omega \nabla \cdot \boldsymbol{g} \, \mathrm{d}\Omega = \oint_{\partial\Omega} \boldsymbol{g} \cdot \boldsymbol{n} \, \mathrm{d}\Gamma, \tag{2.15}$$

to the last term of Eq. (2.14) and inserting the obtained expression into Eq. (2.12) leads to

$$\int_\Omega p' \frac{1}{c_0^2} \frac{\partial^2 p_a}{\partial t^2} \, \mathrm{d}\Omega + \int_\Omega p' \nabla \cdot \nabla p_a \, \mathrm{d}\Omega - \oint_{\partial\Omega} p' \nabla p_a \cdot \boldsymbol{n} \, \mathrm{d}\Gamma = 0, \tag{2.16}$$

where $\partial\Omega$ is the enclosed surface of Ω and $\boldsymbol{n}$ the outwards facing surface normal vector.

In order to uniquely define the pressure p_a in the domain Ω, at least one boundary condition must be specified on the closed boundary surface $\partial\Omega$. A typical boundary condition in the acoustics is the Neumann type, which prescribes a normal traction

$$\nabla p_a \cdot \boldsymbol{n} = p_n = -\rho_0 \frac{\partial \boldsymbol{u_a}}{\partial t} \cdot \boldsymbol{n} = -\rho_0 a_n \tag{2.17}$$

at boundary Γ_n, where a_n denotes the particle acceleration normal to Γ_n. The homogeneous Neumann boundary condition, i.e., $\nabla p_a \cdot \boldsymbol{n} = 0$, is also called sound hard boundary condition and can be used to model acoustic wall. For the inhomogeneous case ($p_n \neq 0$), it acts as an acoustic excitation on the boundary. Another boundary condition is the Dirichlet type, with prescribed pressure

$$p_a = p_i \tag{2.18}$$

at boundary Γ_i. A homogeneous Dirichlet boundary condition ($p_i = 0$) is called sound soft boundary, which occurs mostly at a liquid-gas interface. Note that both sound hard and sound soft boundary conditions can lead to reflection of acoustic waves at the boundary.

Incorporating the Neumann boundary condition Eq. (2.17) into Eq. (2.16), the final weak form is obtained, reading as

$$\int_\Omega p' \frac{1}{c_0^2} \frac{\partial^2 p_a}{\partial t^2} \, \mathrm{d}\Omega + \int_\Omega p' \nabla \cdot \nabla p_a \, \mathrm{d}\Omega = \int_{\Gamma_n} p' p_n \, \mathrm{d}\Gamma, \tag{2.19}$$

which must be satisfied for all test functions p' within the computational domain Ω.

With the same procedure, the weak form of the Helmholtz equation Eq. (2.11) can also be obtained

$$\int_\Omega k^2 p' \hat{p}_a \, \mathrm{d}\Omega - \int_\Omega \nabla p' \cdot \nabla \hat{p}_a \, \mathrm{d}\Omega + \oint_{\partial\Omega} p' \nabla \hat{p}_a \cdot \boldsymbol{n} \, \mathrm{d}\Gamma = 0, \tag{2.20}$$

where k is the wave number, which is the angular frequency divided by the speed of sound. Again, the Neumann boundary condition

$$\nabla \hat{p}_a \cdot \boldsymbol{n} = \hat{p}_n \tag{2.21}$$

at boundary Γ_n or the Dirichlet boundary condition

$$\hat{p}_a = \hat{p}_i \tag{2.22}$$

at boundary Γ_i can be incorporated.

2.2 Modeling of open domain problem

To model exterior acoustics problems in which the acoustic wave propagates in an open unbounded domain, special care needs to be taken. A common practice is to truncate the propagation domain at a finite distance from the source and use homogeneous Neumann or Dirichlet boundary conditions, but this will result in an undesired reflection of the outgoing wave at the boundary [11, 19]. One solution to such an open-domain problem is to apply a special condition at the boundary, the so-called absorbing boundary condition (ABC), which was first introduced by Engquist and Majda in 1977 [20]. The other commonly used domain truncation technique is the perfectly matched layer (PML), which is an additional acoustic domain surrounding the propagation domain, in which the acoustic waves are damped. The name "perfectly matched" refers to the matching impedances of both domains, and hence no reflections of the impinging wave occur at the domain boundary. Its concept was first introduced by Berenger in 1994 [21] and was originally designed for the electromagnetic problem. There has been much research work on the PML-technique [11], and it is currently widely used in acoustic, electromagnetic or elastodynamic simulation [19]. In the following, the basic concept of the PML technique is explained closely following Kaltenbacher [11, 22].

We consider the linear wave equation Eq. (2.8) for one dimensional case with spatial coordinate x, which reads as

$$\frac{1}{c_0^2}\frac{\partial^2 p_a}{\partial t^2} - \frac{\partial^2 p_a}{\partial x^2} = 0. \tag{2.23}$$

For plane wave propagation, the reflection coefficient R at the interface between the propagation domain and the PML domain computes as

$$R = \frac{Z_{\mathrm{pml}} - Z_0}{Z_{\mathrm{pml}} + Z_0}, \tag{2.24}$$

with $Z_{\mathrm{pml}} = \tilde{\rho}\tilde{c}$ the acoustic impedance in the PML region and $Z_0 = \rho_0 c_0$ the specific acoustic impedance of the propagation medium, respectively. In order to make $R = 0$ achieve zero reflection at the interface, Z_{pml} has to match Z_0. Since the PML is an artificial domain, the two quantities $\tilde{\rho}$ and $\tilde{c}$ are free to be chosen in such a way that just their product equals $\rho_0 c_0$. By choosing complex values like

$$\tilde{\rho} = \rho_0(1 - j\sigma_x); \qquad \tilde{c} = \frac{c_0}{1 - j\sigma_x}, \tag{2.25}$$

the impedance matching $Z_{\mathrm{pml}} = Z_0$ is still achieved. Here, σ_x denotes a damping function in x-direction and will be explained later in more detail. Furthermore, we consider the one dimensional Helmholtz equation, which is the time-harmonic case of Eq. (2.23) and formulate for the PML region, we obtain

$$\frac{\omega^2}{\tilde{c}^2}\hat{p}_a + \frac{\partial^2 \hat{p}_a}{\partial x^2} = 0. \tag{2.26}$$

The first term in Eq. (2.26) can also be expressed by a complex wave number $\tilde{k}$

$$\tilde{k} = \frac{\omega}{\tilde{c}} = \frac{\omega}{c_0}(1 - j\sigma_x) = k(1 - j\sigma_x). \tag{2.27}$$

The general solution for the pressure in the PML region then reads as

$$p_a(x,t) = Re\{\hat{p}_a e^{j(\omega t - \tilde{k}x)}\} = Re\{\hat{p}_a e^{j(\omega t - kx)} e^{-\sigma_x kx}\}. \tag{2.28}$$

If σ_x is chosen as constant, the pressure amplitude is decreased by the real term $e^{-\sigma_0 kx}$ with rising x, hence the acoustic wave is damped.

The formulation of PML so far works only for cases where the impinging wave is normal to the interface between both regions. However, if the wave impinges to the normal vector of the interface at an angle ϕ, then the acoustic impedances compute by

$$Z_0 = \frac{\rho_0 c_0}{\sin(\phi_1)} \qquad Z_{\mathrm{pml}} = \frac{\tilde{\rho}\tilde{c}}{\sin(\phi_2)}, \tag{2.29}$$

and the method will not work. Therefore, we need to split the linearized conservation equations Eq. (2.5) and Eq. (2.6) into their spatial directions and introduce for each direction an artificial damping individually, which leads to the modified Helmholtz equation

$$\eta_y\eta_z \frac{\partial}{\partial x}\left(\frac{1}{\eta_x}\frac{\partial \hat{p}_a}{\partial x}\right) + \eta_x\eta_z \frac{\partial}{\partial y}\left(\frac{1}{\eta_y}\frac{\partial \hat{p}_a}{\partial y}\right) + \eta_x\eta_y \frac{\partial}{\partial z}\left(\frac{1}{\eta_z}\frac{\partial \hat{p}_a}{\partial z}\right) + \eta_x\eta_y\eta_z k^2 \hat{p}_a = 0, \tag{2.30}$$

where the functions

$$\eta_i = 1 - j\frac{\sigma_i}{\omega}, i \in \{x,y,z\} \tag{2.31}$$

were introduced, with σ_i being the damping functions in the spatial direction $i \in \{x,y,z\}$. The full derivation of Eq. (2.30) can be found in [11]. A second method to derive Eq. (2.30) is the so-called complex coordinate stretching, which maps the solution of the Helmholtz equation in the real coordinate space to a complex coordinate space. This is done by defining the mapping, e.g., for x

$$\tilde{x}(x) = x + \frac{1}{j\omega}\int_0^x \sigma_x(\tilde{x})\,\mathrm{d}\tilde{x}, \tag{2.32}$$

and thus, the derivative of the stretched coordinate $\tilde{x}$ with respect to its original x is then

$$\frac{\partial \tilde{x}}{\partial x} = 1 + \frac{\sigma_x}{j\omega} = \eta_x. \tag{2.33}$$

The derivative Eq. (2.33) can be transformed as

$$\frac{\partial}{\partial \tilde{x}} = \frac{1}{\eta_x}\frac{\partial}{\partial x}. \tag{2.34}$$

In the case of $\sigma_i = 0$, the stretched and the original coordinates are the same and $\eta_i = 1$, i.e., no mapping. Applying the coordinate stretching to all direction components, we obtain the operator

$$\tilde{\nabla} = \left(\frac{1}{\eta_x}\frac{\partial}{\partial x}, \frac{1}{\eta_y}\frac{\partial}{\partial y}, \frac{1}{\eta_z}\frac{\partial}{\partial z}\right)^T. \tag{2.35}$$

Inserting the operator Eq. (2.35) into the Helmholtz equation Eq. (2.11) leads to the modified Helmholtz equation Eq. (2.30).

In the following, the damping function σ_i will be discussed in more detail. The performance of the PML depends on the choice of the damping function. Different damping functions are shown in [11]. However, it can be proven that using a function that is zero at the interface between the propagation region and PML region and grows towards infinity with $\tilde{x} \to L$ works optimally for the Helmholtz equation [11, 22]. Such function is called inverse distance function and can be written as

$$\sigma_x = \frac{c_0}{L - \tilde{x}}. \tag{2.36}$$

Here, c_0 denotes the speed of sound in the propagation domain, L denotes the thickness of the PML and the PML coordinate $\tilde{x}$ is zero at the domain interface and L at the end of the layer. The speed of sound in the numerator is used for eliminating the dependency on c_0 in the damping term, which has the form $e^{-\sigma_x kx} = e^{-\sigma_x \frac{\omega}{c_0} x}$ (see Eq. (2.28)). Another possibility besides using a constant damping function

$$\sigma_x = \sigma_0 c_0 \tag{2.37}$$

is to use a quadratic increase damping function like

$$\sigma_x = \sigma_0 c_0 \frac{\tilde{x}^2}{L^2}, \tag{2.38}$$

in this case, the constant damping factor σ_0 needs to be chosen carefully for the given PML thickness L. Setting the damping factor too low could lead to insufficient damping of the acoustic wave in the PML domain, while setting it too high may cause numerical issues [22]. The tuning of the parameter is not necessary when using the inverse distance damping function, since it is dependent on the PML thickness L. A decreased thickness of the PML can be compensated by a higher value of the damping factor, but there is a limit where discretization errors become dominant [22]. Therefore, even for the optimal damping function, the thickness of the PML has to be chosen properly. Kaltenbacher [22] achieved good results with a PML thickness $t_{\mathrm{PML}} = \frac{\lambda}{4}$ and $t_{\mathrm{PML}} = \frac{\lambda}{8}$ in dependence of the acoustic wavelength $\lambda = \frac{c_0}{f}$ with a total error of 0.1% in the propagation region. Furthermore, using a minimum of two linear elements or one quadratic element to resolve the PML region and choosing a similar element size for the propagation region and the PML region were suggested.

2.3 Fundamentals of noise measurement

In this section, the most important terminologies in the noise and sound measurement technique will be briefly explained.

2.3.1 Sound level

The hearing of humans does not respond linearly to acoustic pressure; hence, a logarithmic scale is introduced when measuring the acoustic quantities [15]. The most commonly measured physical attribute of the sound is the sound pressure. Other important measures are sound particle velocity, sound intensity, and sound power. The definitions of the logarithmic measures of the above-mentioned quantities are presented below, following Kaltenbacher [12] and Heutschi [14].

Sound pressure level

The sound pressure level (SPL) is defined as

$$L_p = 10 \log_{10} \frac{p_{a,\mathrm{rms}}^2}{p_{\mathrm{ref}}^2} = 10 \log_{10} \frac{p_{a,\mathrm{rms}}}{p_{\mathrm{ref}}} \, \mathrm{dB}, \tag{2.39}$$

where $p_{\mathrm{ref}} = 2 \cdot 10^{-5}$ Pa denotes the reference sound pressure, which is often considered as the threshold of human hearing at 1000 Hz [23]. The quantity $p_{a,\mathrm{rms}}$ is the root-mean-square value of the acoustic pressure and is also called the effective pressure, which is defined as the square root of the average of the square of the pressure of the sound signal over a given time duration T and reads as

$$p_{a,\mathrm{rms}} = \sqrt{\frac{1}{T} \int_{t_0}^{t_0+T} p_a^2(t) \, \mathrm{d}t}. \tag{2.40}$$

It can be shown that for a sinusoidal acoustic wave like Eq. (2.10), the effective pressure can be expressed as [24]

$$p_{a,\mathrm{rms}} = \frac{\hat{p}_a}{\sqrt{2}}. \tag{2.41}$$

Sound velocity level

Further, the sound velocity level (SVL) or the particle velocity level is defined as

$$L_u = 10 \log_{10} \frac{u_{a,\mathrm{rms}}^2}{u_{\mathrm{ref}}^2} = 10 \log_{10} \frac{u_{a,\mathrm{rms}}}{u_{\mathrm{ref}}} \, \mathrm{dB}, \tag{2.42}$$

with $u_{\mathrm{ref}} = 5 \cdot 10^{-8} \, \frac{m}{s}$ the reference particle velocity in air and $u_{a,\mathrm{rms}}$ the root-mean-square particle velocity. Again, the effective particle velocity can be expressed as

$$u_{a,\mathrm{rms}} = \frac{\hat{u}_a}{\sqrt{2}} \tag{2.43}$$

for sinusoidal acoustic waves.

Sound intensity level

The instantaneous acoustic intensity $\boldsymbol{I_a}$ is defined by the product of the acoustic pressure and the particle velocity

$$\boldsymbol{I_a} = p_a \boldsymbol{u_a}. \tag{2.44}$$

For the sound intensity level (SIL), the averaged value of the instantaneous acoustic intensity is used, which is computed as

$$I_a^{\mathrm{ave}} = |\boldsymbol{I}_{\boldsymbol{a}}^{\mathrm{ave}}| = \left| \frac{1}{T} \int_{t_0}^{t_0+T} p_a \boldsymbol{u}_{\boldsymbol{a}} \,\mathrm{d}t \right| . \tag{2.45}$$

The sound intensity level is then defined as

$$L_I = 10 \log_{10} \frac{I_a^{\mathrm{ave}}}{I_{\mathrm{ref}}} \,\mathrm{dB}, \tag{2.46}$$

with $I_{\mathrm{ref}} = 10^{-12}\,\mathrm{W/m^2}$ the reference sound intensity corresponding to the product of the reference sound pressure p_{ref} and the reference particle velocity u_{ref}.

Sound power level

The acoustic power is obtained by integrating the acoustic intensity over a closed surface and reads as

$$W_a = \oint_\Gamma \boldsymbol{I}_{\boldsymbol{a}} \cdot \,\mathrm{d}\boldsymbol{s} = \oint_\Gamma \boldsymbol{I}_{\boldsymbol{a}} \cdot \boldsymbol{n} \,\mathrm{d}s, \tag{2.47}$$

with $\boldsymbol{n}$ being the surface normal vector. The sound power level (SWL) is then defined as

$$L_W = 10 \log_{10} \frac{W_a^{\mathrm{ave}}}{W_{\mathrm{ref}}} \,\mathrm{dB}, \tag{2.48}$$

with $W_{\mathrm{ref}} = 10^{-12}\,\mathrm{W}$ being the reference sound power and W_a^{ave} the averaged value of the acoustic power, which is computed for the time harmonic case using

$$\begin{aligned} W_a^{\mathrm{ave}} &= \int_\Gamma \left(\frac{1}{T} \int_{t_0}^{t_0+T} Re\{\hat{p}_a e^{j\omega t}\}\, Re\{\hat{\boldsymbol{u}}_{\boldsymbol{a}} \cdot \boldsymbol{n} e^{j\omega t}\} \,\mathrm{d}t \right) \mathrm{d}s & (2.49) \\ &= \frac{1}{2} \int_\Gamma Re\{\hat{p}_a \hat{\boldsymbol{u}}_{\boldsymbol{a}}^*\} \cdot \boldsymbol{n} \,\mathrm{d}s, & (2.50) \end{aligned}$$

with $()^*$ denoting the complex conjugate.

2.3.2 Octaves and frequency bands

A noise signal is often analyzed in the frequency domain in order to assess its frequency content. The frequency spectrum is divided into various frequency bands covering the hearing range of humans, which varies from 20 Hz to 20 000 Hz. The most commonly used frequency bands in acoustic measurement are octave bands and one-third octave bands.

Octave band

An octave band has a frequency span ratio of 2:1, which means that the upper limit frequency f_u of the band is twice its lower limit frequency f_l, i.e.,

$$f_u = 2 f_l \, . \tag{2.51}$$

The center frequency f_m of the octave band is then calculated by their geometric mean

$$f_m = \sqrt{f_l f_u} = \sqrt{2} f_l \, . \tag{2.52}$$

The bandwidth Δf of the octave band is given by

$$\Delta f = f_u - f_l = \frac{f_u}{2} = \frac{f_m}{\sqrt{2}} \, . \tag{2.53}$$

For acoustic measurements, the human audible range is split into ten octave bands, with center frequencies being 31.5, 63, 125, 250, 500, 1000, 2000, 4000, 8000 and 16000 Hz.

Fractional octave bands

If more detailed information about the frequency content of the noise is needed, fractional octave bands with higher frequency resolution can be used. In general, for a 1/n-octave band, the relation between the upper and the lower frequency limit is defined as

$$f_u = 2^{\frac{1}{n}} f_l \, . \tag{2.54}$$

And the center frequency of 1/n-octave band is given by

$$f_m = \sqrt{f_l f_u} = 2^{\frac{1}{2n}} f_l \, . \tag{2.55}$$

One can see that for $n = 1$, the same expressions are obtained as those for the octave band.

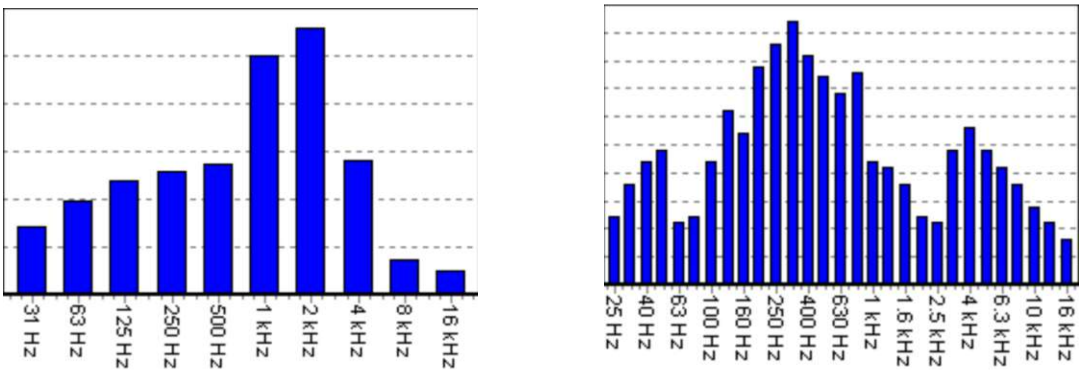

Figure 2.1: Example octave band and 1/3-octave band spectra. Left: octave band spectrum. Right: 1/3-octave band spectrum. [2]

A widely used fractional octave band in the acoustic measurement is the 1/3-octave band, which is obtained by splitting each of the octave bands into three parts. Example sound spectra given in octave bands and 1/3-octave bands are shown in Fig. 2.1. It can be seen that the spectrum in 1/3-octave bands contains more frequency bands than that of the octave band, allowing a more detailed analysis of the frequency content of the noise. Other common narrower fractional octave bands are for example 1/6-octave, 1/12-octave and 1/24-octave bands.

2.3.3 Frequency weighting

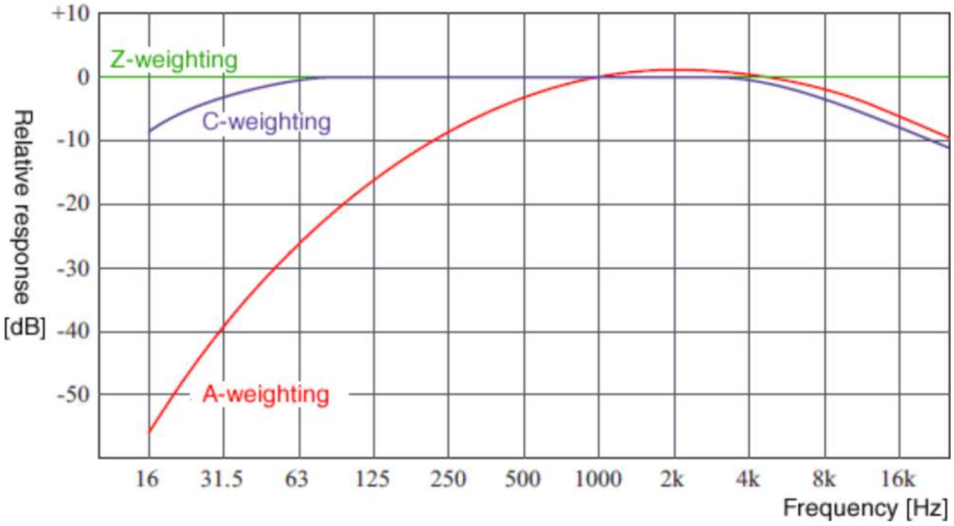

Figure 2.2: Frequency weighting (A, C and Z) [3].

The human audible system does not respond equally to sound frequencies. It is more sensitive to frequencies between 500 Hz and 8000 Hz and less sensitive to lower pitch and higher pitch noises [25]. To match this frequency-dependent perception of sound loudness of the human ear, frequency weighting filters have been defined, which can be seen as correction functions of the measured sound levels. However, the frequency response of the ear also depends on sound pressure level, at lower levels of pressure the effect is more pronounced than at higher levels [14]. Therefore, several weighting filters have been defined. The most commonly used weighting functions are A-weighting and C-weighting, which are designed for low and high sound levels, respectively. If no weighting filter is applied to the measurement, it is also called Z-weighting. The response functions of the A, C and Z-weighting filters are shown in Fig. 2.2.

In the ambient noise measurement, the most frequently used weighting is A-weighting. It can be calculated by the weighting function [26]

$$R_A(f) = \frac{12194^2 f^4}{(f^2 + 20.6^2)\ \sqrt{(f^2 + 107.7^2)\,(f^2 + 737.9^2)}\ \ (f^2 + 12194^2)}\,, \tag{2.56}$$

with f being the frequency in Hz, the amplitude response of A-filter results in

$$\text{A-weighting}(f) = 20\log_{10}\left(R_A(f)\right) - 20\log_{10}\left(R_A(1000)\right)\ . \tag{2.57}$$

The second term in Eq. (2.57) is to ensure that the amplitude of the weighting function is normalized to 0 dB at 1000 Hz, which can also be seen in Fig. 2.2. Sound level measurements with A-weighting filter applied are expressed as dBA, or dB(A).

2.4 X-Wagen metro train

In this thesis, the finite element modeling approach of underfloor noise prediction is applied to the X-Wagen metro from Siemens Mobility. A brief overview of the metro train is presented in the following section in order to provide a better insight into the modeled vehicle.

Figure 2.3: The first X-Wagen metro train at Siemens Mobility plant Leberstraße [4].

The metro train Type X, also known as the X-Wagen, was developed by Siemens and is manufactured at the Siemens Mobility plant in Vienna. The third generation of the Vienna metro system aims to replace the old metro model Silberpfeil, which has been in operation since 1972. Siemens delivered the first X-Wagen (Fig. 2.3) in 2020, and the last vehicle is scheduled for delivery at the end of 2030.

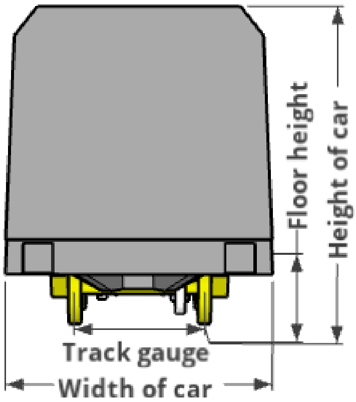

(a) Front view

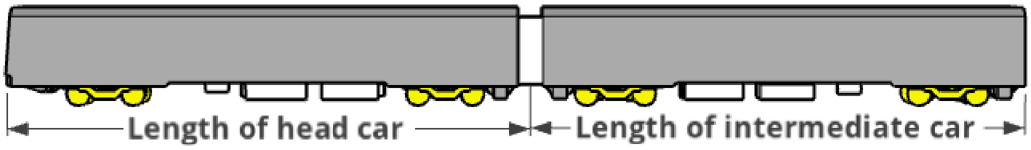

(b) Side view

Figure 2.4: Simplified 3D model of the X-Wagen in its basic configuration.

The basic configuration of the train, as shown in Fig. 2.3 and Fig. 2.4b, consists of two metro cars, a non-motorized head car where the driver's cab is located, and a motorized intermediate car. One section of the metro car is about 2.85 m in width and 3.6 m in height and they have lengths of 19.1 m for the head car and 18.3 m for the intermediate car, respectively. The train has a standard track gauge of 1.425 m, and the car floor is about 0.95 m over top of the rail. In the operating configuration, the metro train is made up of six sections consisting of two head cars and four intermediate cars with a length of over 110 m.

Figure 2.5: A non-driven bogie from the head car. The main components are numbered as follows; (1) bogie frame, (2) wheel and axle, (3) brake disc, (4) air suspension.

The main components in the train underfloor are the bogies and other supporting units like air compressors, electrical transformers, etc. Each metro car is equipped with two bogies. While the bogies at the front car are non-driven, the intermediate car bogies are driven by traction motors. A non-driven bogie from the front car is shown in Fig. 2.5 with the main components numbered. These are the bogie frame with a length of about 3 m, the wheels with 0.85 m diameter at a distance of 2 m from each other, the axles, and the air suspensions. Each axle is equipped with one brake disk and one brake caliper unit, and the brake components of both axles are arranged in an anti-symmetric order.

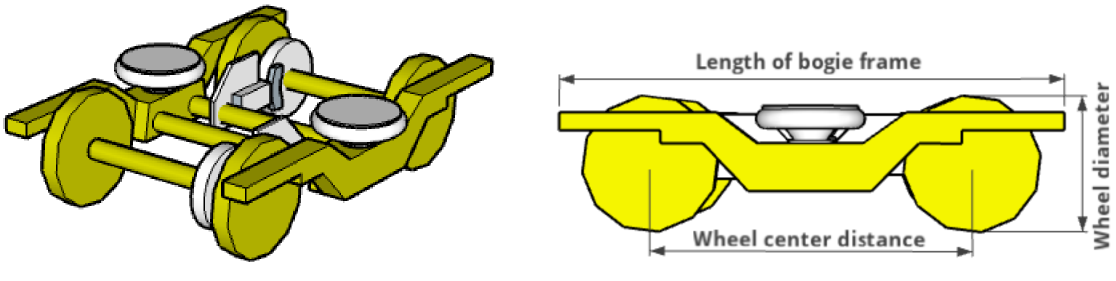

(a) Perspective view

(b) Side view

Figure 2.6: Simplified 3D model of the non-driven bogie containing the main components as described in Fig. 2.5.

A simplified 3D model of the non-driven bogie containing the mentioned main components is shown in Fig. 2.6. One can see that the brake components introduce asymmetry into the bogie geometry. If they are disregarded, the symmetry of the bogie can be exploited, and the full model can be represented by a one-fourth model, which is used in the latter finite element modeling in Chapter 4. Finally, the mentioned dimensions of the metro car and of the bogie components in this section are summarized in

Tab. 2.1.

Table 2.1: Dimensions of metro car and bogie as shown in Fig. 2.4 and Fig. 2.6b.

Parameter	Dimension (mm)
Metro car	
Width of car	2,850
Height of car	3,588
Length of head car	19,125
Length of intermediate car	18,250
Floor height above top of rail	948
Track gauge	1,435
Bogie	
Length of bogie frame	3,076
Wheel center distance	2,000
Wheel diameter	850

Chapter 3

Measurements

In order to be able to validate the results obtained from the finite element simulation (see Chapter 5), specific measurements have been carried out. In this chapter, the acoustic power measurement of the sound source and the outer pressure field measurement around the car body are presented. The resulting sound power spectrum of the omnidirectional loudspeaker provides simulation input for the finite element analysis in section 4.2. Furthermore, the measurement results of outer pressure field serve as validation for the finite element model in Chapter 5.

3.1 Characterization of sound source

Two important characteristics of a sound source are directivity and sound power. For the validation measurement, a dodecahedron loudspeaker, type Brüel & Kjaer 4292-L, is used as excitation, which can be treated as an omnidirectional sound source. Hence, only the sound power emitted by the loudspeaker is interesting. In the following, the acoustic power spectrum of the sound source is measured following ISO 9614-2 [5].

Measurement setup

In Fig. 3.1 the measurement setup for the determination of sound power levels is shown. The omnidirectional loudspeaker was placed on a reflective concrete floor and was enveloped by a 1m x 1m x 1m reference box. The loudspeaker was driven by a reference amplifier with pink noise as an input signal (Fig. 3.2). In order to reduce fluctuations in output power, the amplifier was switched on and warmed up for at least 20 minutes before the start of the measurement. The measurement was carried out according to the ISO 9614-2 standard, in which the sound power is determined from intensity measurement over measurement surfaces. This method has the advantage that room reflections and any sound sources outside of the reference box do not influence the measurement result. The intensity measurements were done using the Brüel & Kjaer sound intensity probe kit type 3654, which includes a pair of microphones that are placed face to face with each other, separated by a spacer.

This method of intensity measurement is also called two-microphone method or $p-p$ method. Instead of direct measurement, the particle velocity is obtained by a finite-difference approximation to the pressure gradient [27, 28]. In the following, the basic concept of sound power measurement using the two-microphone method is shown. The relation between particle velocity $\boldsymbol{u_a}$ and the acoustic pressure p_a is described by the Euler equation of motion,

$$\rho_0 \frac{\partial \boldsymbol{u_a}}{\partial t} = -\nabla p_a. \tag{3.1}$$

In the intensity measurement using the two-microphone method (Fig. 3.3), the intensity probe is moved over the measurement surface with a constant speed and is kept perpendicular to the scanned area so that only the normal component of the particle velocity is captured. Furthermore, the normal component of the pressure gradient in Eq. (3.1) is approximated by the finite difference of the measured pressures. Equation (3.1) for the normal component then reads as

$$\rho_0 \frac{\partial(\boldsymbol{u_a} \cdot \boldsymbol{n})}{\partial t} = -\nabla p_a \cdot \boldsymbol{n} \approx -\frac{p_2 - p_1}{\Delta r}, \tag{3.2}$$

with p_1 and p_2 being the measured pressure of the microphone closer and further from the incident sound wave, respectively, Δr being the thickness of the spacer, and $\boldsymbol{n}$ the unit normal vector of the measurement surface. Hence, the normal particle velocity u_n can be expressed as

$$u_n = \boldsymbol{u_a} \cdot \boldsymbol{n} = \int \frac{(p_1 - p_2)}{\rho_0 \Delta r} \, \mathrm{d}t. \tag{3.3}$$

The normal component of the sound intensity is then obtained by the product of the approximated particle velocity and the mean of the measured pressures

$$I_n = \boldsymbol{I_a} \cdot \boldsymbol{n} = p_a u_n = \frac{p_1 + p_2}{2} \int \frac{(p_1 - p_2)}{\rho_0 \Delta r} \, \mathrm{d}t. \tag{3.4}$$

Each partial measurement surface is scanned twice, using a vertical and a horizontal scan path, respectively. The obtained result is the spatially averaged intensity $\langle I_n \rangle$. The sound power of a single measurement surface is then given by the product of the spatial average intensity and the surface area by

$$W_i = \langle I_{n,i} \rangle S_i \,. \tag{3.5}$$

The total sound power of the enclosed sound source is then given by the sum of the sound power of each measurement surface and reads as

$$W_{total} = \sum_{i=1}^{N} W_i \,. \tag{3.6}$$

Figure 3.1: Setup for sound power measurement.

(a) Inter-M R300 Plus reference amplifier

(b) NTI Minirator MR-PRO

Figure 3.2: Signal generator and amplifier.

Figure 3.3: Intensity measurement using the two-microphone method according to ISO 9614-2 [5].

Measurement results

The measurement is post-processed using the Brüel & Kjaer type 2270 hand-held analyzer and the result is shown in one-third octave band spectra. Figure 3.4 shows the measured non-weighted (Z-weighting) sound power level (SWL ref 1 pW) from 100 Hz to 2000 Hz. The measurement was carried out twice, and the deviation of both measurements was within 0.3 dB in total power. For the finite element simulation, the averaged value of both measurements as shown in Fig. 3.4c was used.

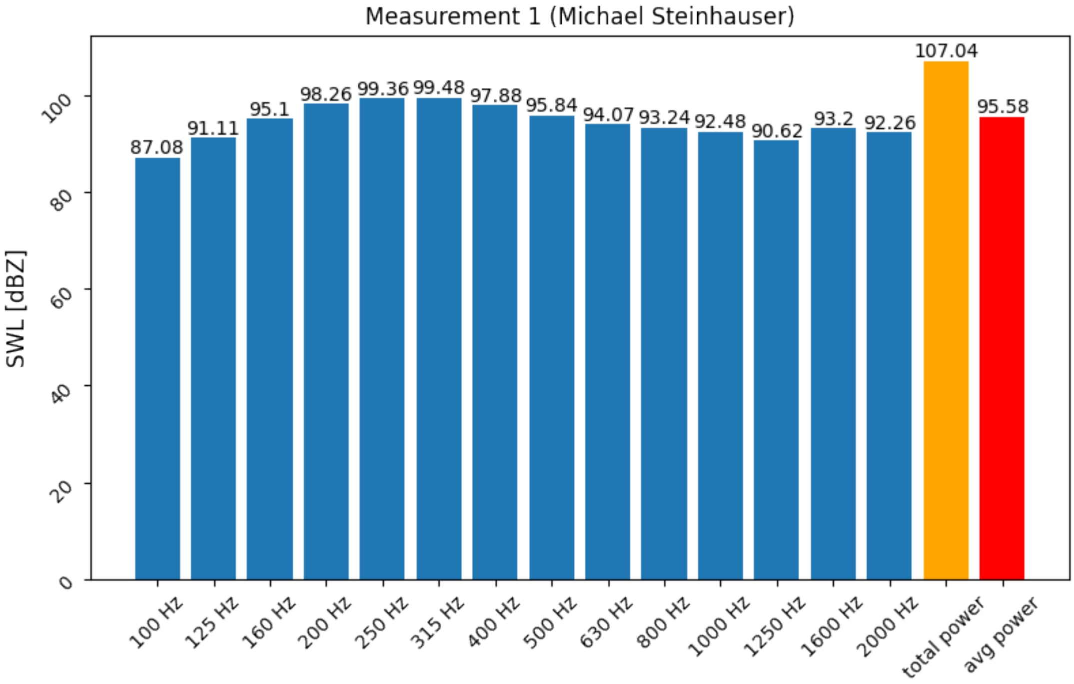

(a) Measurement series 1

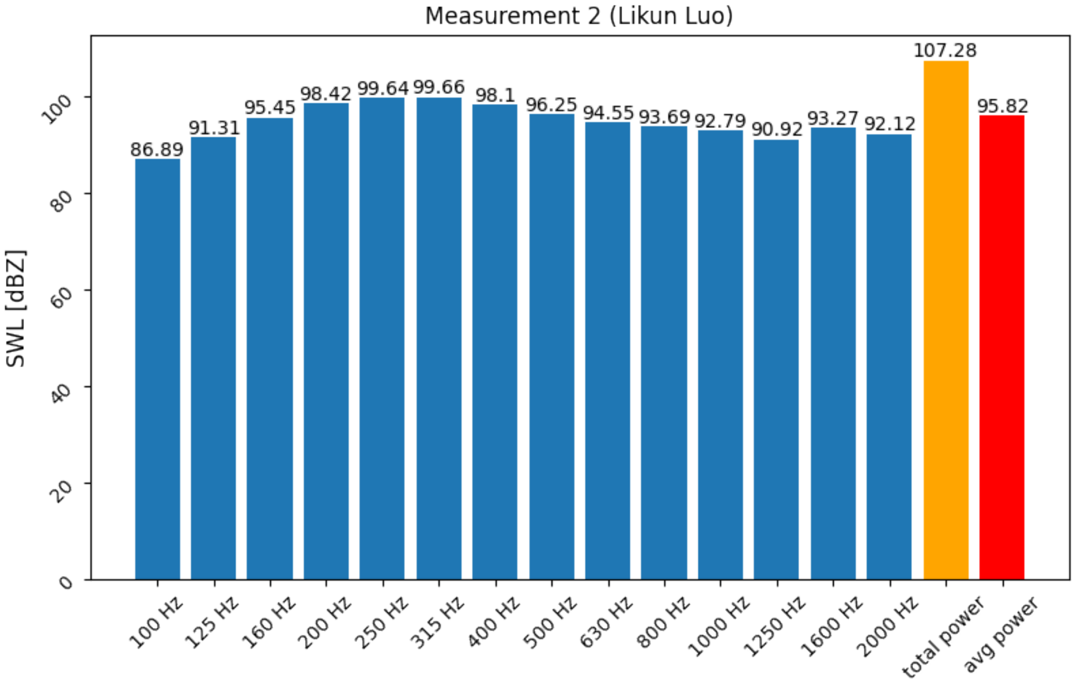

(b) Measurement series 2

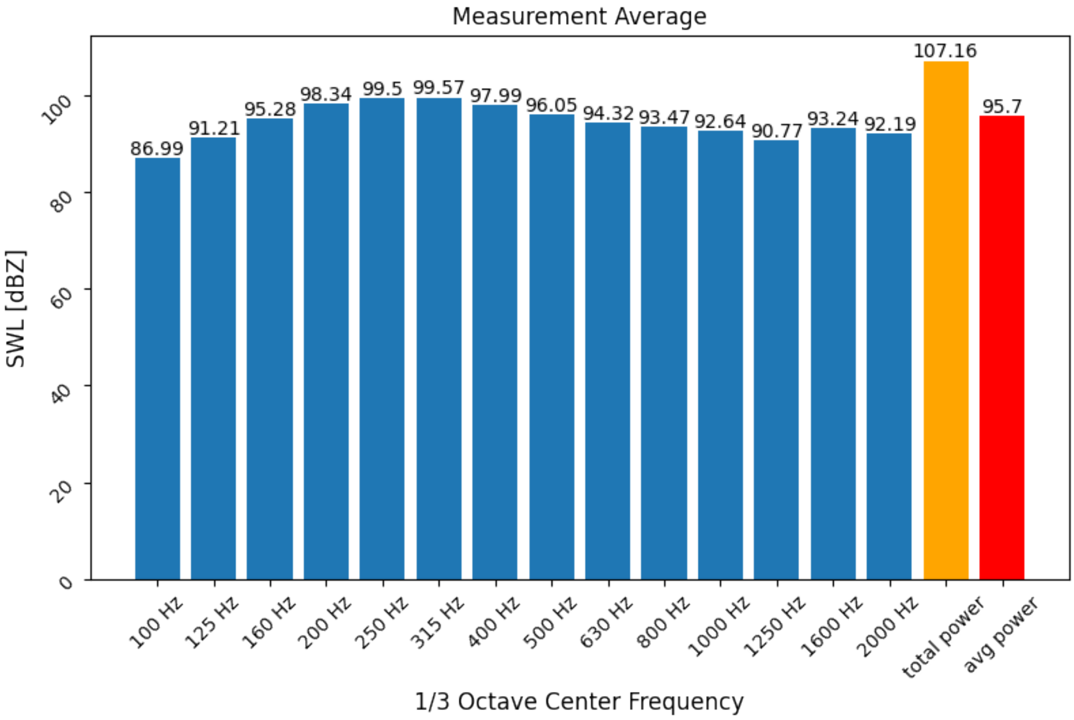

(c) Averaged value of both measurement series

Figure 3.4: Sound power spectra in 1/3-octave bands, SWL in dB ref 1 pW.

3.2 Pressure field measurement on a standing metro train

In this section, we describe the sound pressure measurements, which were done on a standing UBX metro with controlled excitation. The reason to perform measurements under standstill conditions was to avoid the uncertainties introduced by the complex real sources (e.g., wheel-rail interaction) in dynamic conditions. With this approach, the quality of the finite element model can be better assessed.

Measurement setup

The measurement was performed on October 4, 2022, at the company premises of Siemens Mobility Austria in 1110 Vienna. The measurement setup is shown in Fig. 3.5. Figure 3.5a shows the front car of the measurement vehicle of type Siemens U-Bahn Wien X. In order to approximate free field conditions as closely as possible, the measurement vehicle was parked in a relatively empty area of the company premises to avoid environmental reflections as much as possible.

To evaluate the outer pressure field close to the car body, 10 pressure microphones were arranged in a line array order, allowing simultaneous measurement along the height direction. As shown in Fig. 3.5b, the microphones were attached on a tripod at a distance of half a meter to each other, the position of the microphones started at 0.5 m and ended at 5 m above ground.

The acoustic excitation came from an omnidirectional loudspeaker with pink noise as an input signal, using identical settings as in the previous acoustic power measurement. The loudspeaker was placed beneath the car underframe in the empty space between the bogie axle and the wheel axle, at about 55 cm above the ground (see Fig. 3.6). Measurements were performed with two different loudspeaker locations: one at the front of the bogie (Position A) and the other at the rear (Position B), as marked in Fig. 3.5b. The aim was to evaluate the possible asymmetric effect caused by the anti-symmetric layout of the bogie components (e.g., brake discs); also, it provides validation for the finite element model, which will exploit the symmetry using the image-source technique.

Due to the limited availability of the measurement vehicle, the measurement was concentrated on only one side of the vehicle near the front bogie. In Fig. 3.7, all measurement positions of the microphone array are shown and labeled. Position a is the starting position of measurement, it lies on the centerline of the bogie frame, 10 cm away from the carbody edge (see Fig. 3.7b). The full description of measurement positions is found in Tab. 3.1.

Position	Description
a	on bogie centerline, 10 cm away from carbody edge
b	50 cm out of bogie centerline in front direction, 10 cm away from carbody edge
c	100 cm out of bogie centerline in front direction, 10 cm away from carbody edge
d	50 cm out of bogie centerline in rear direction, 10 cm away from carbody edge
e	100 cm out of bogie centerline in rear direction, 10 cm away from carbody edge
f	on bogie centerline, 50 cm away from carbody edge
g	on bogie centerline, 100 cm away from carbody edge
h	on bogie centerline, 150 cm away from carbody edge
i	on bogie centerline, 200 cm away from carbody edge

Table 3.1: Description of measurement positions.

At each measurement position, the multi-channel time-varying signal of the pressure field was captured by the Müller-BBM PAK MKII data acquisition system. The duration of a single measurement run was set to 15 seconds. The captured time signal will be post-processed using the provided Müller-BBM PAK software suite.

(a) Front view

(b) Side view

Figure 3.5: Outer pressure field measurement setup.

(a) Position A: front of the bogie

(b) Position B: rear of the bogie

Figure 3.6: Loudspeaker locations.

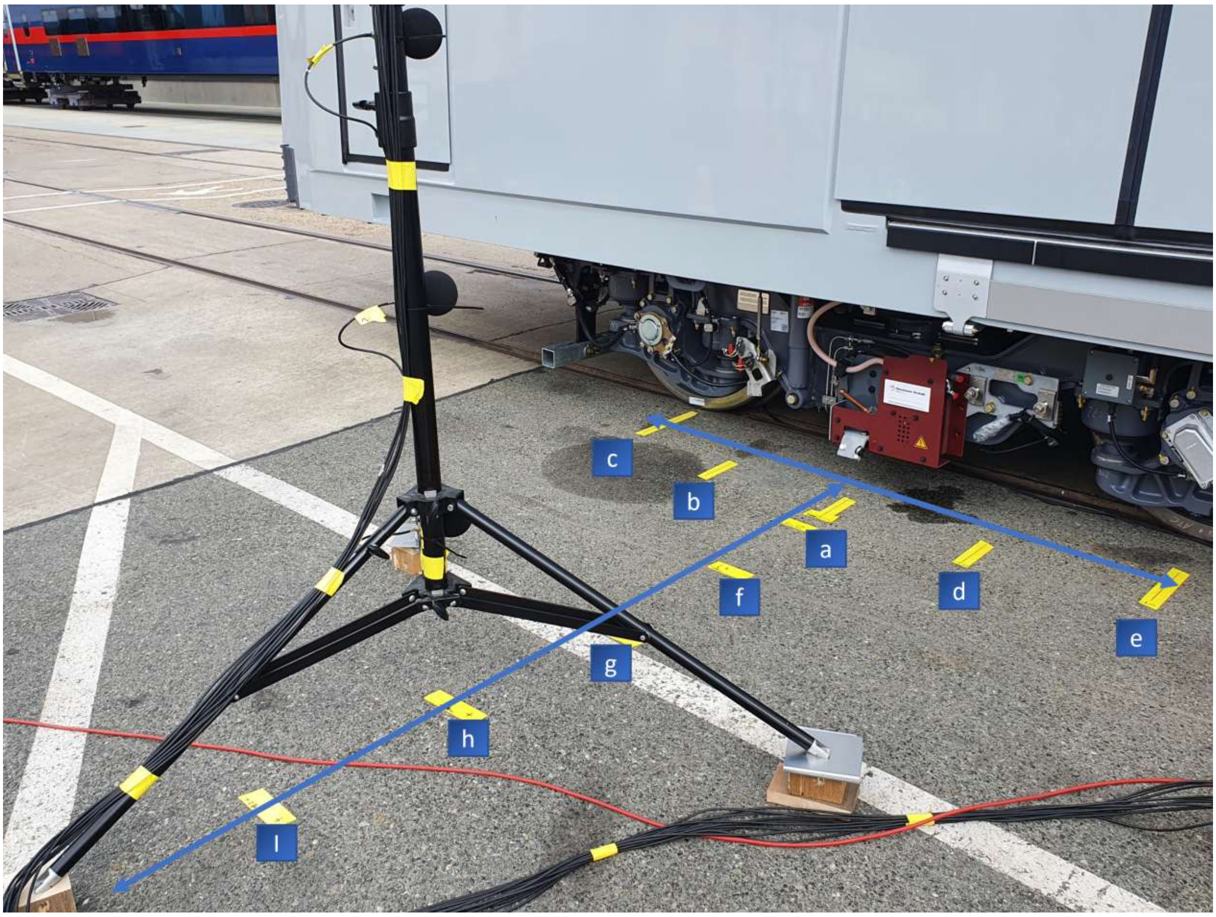

(a) Measurement positions a to i

(b) Position a: centerline of the bogie, 10 cm away from carbody edge

Figure 3.7: Measurement positions of microphone array.

Measurement results

In Fig. 3.8a, the measured time signal of microphone 1 (0.5 m above ground) at measurement position a (front bogie centerline, 10 cm away from car body) with loudspeaker placed at the front of the bogie are shown. The signal was converted into frequency domain using Fourier transformation as shown in Fig. 3.8b. The post-processing was done directly in the provided software suit Müller-BBM PAK 6.x. Figure 3.9 shows a screenshot of the software GUI and the FFT parameters used are circled.

In Fig. 3.8b, the blue curve shows the amplitude of acoustic pressure in narrow band resolution. The narrow band data was converted to 1/n octave form by summing up the amplitude of narrow-band spectral lines contained within the corresponding frequency bandwidth. The advantage of post-processing the data into octave bands is that it provides clearer information about the frequency composition of the noise signal. For example, it can be observed that in the 1/3 octave curve in Fig. 3.8b, the peak of the SPL appears at 315 Hz, which also matches the peak in the SWL spectrum of the sound source as shown in Fig. 3.4c.

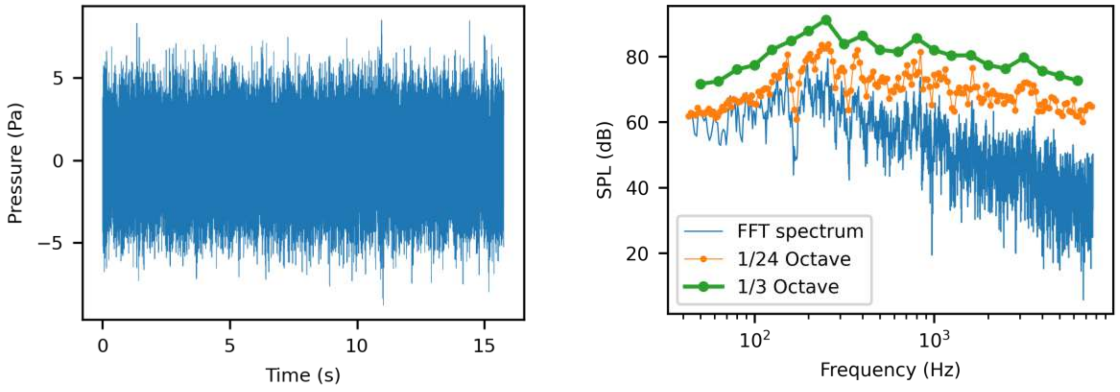

(a) Time domain

(b) Frequency domain

Figure 3.8: Measurement data at measurement position a, at 0.5 m height above ground, loudspeaker located at the front of the bogie.

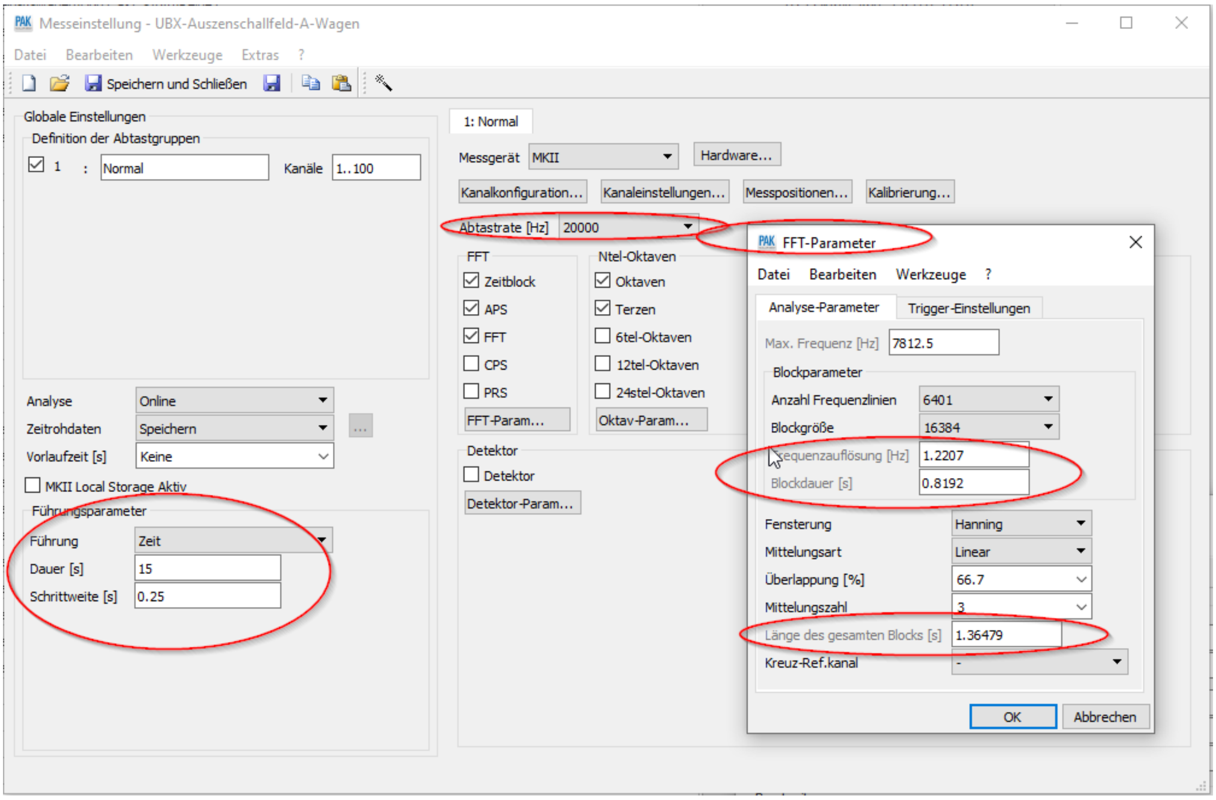

Messeinstellung - UBX-Auszenschallfeld-A-Wagen

Datei Bearbeiten Werkzeuge Extras ?

Speichern und Schließen

Globale Einstellungen

Definition der Abtastgruppen

☑ 1 : Normal Kanäle 1..100

Analyse: Online

Zeitrohdaten: Speichern

Vorlaufzeit [s]: Keine

☐ MKII Local Storage Aktiv

Führungsparameter

Führung: Zeit

Dauer [s]: 15

Schrittweite [s]: 0.25

1: Normal

Messgerät: MKII

Abtastrate [Hz]: 20000

FFT

☑ Zeitblock

☑ APS

☑ FFT

☐ CPS

☐ PRS

Ntel-Oktaven

☑ Oktaven

☑ Terzen

☐ 6tel-Oktaven

☐ 12tel-Oktaven

☐ 24stel-Oktaven

Detektor

☐ Detektor

FFT-Parameter

Datei Bearbeiten Werkzeuge ?

Analyse-Parameter | Trigger-Einstellungen

Max. Frequenz [Hz]: 7812.5

Blockparameter

Anzahl Frequenzlinien: 6401

Blockgröße: 16384

Frequenzauflösung [Hz]: 1.2207

Blockdauer [s]: 0.8192

Fensterung: Hanning

Mittelungsart: Linear

Überlappung [%]: 66.7

Mittelungszahl: 3

Länge des gesamten Blocks [s]: 1.36479

Kreuz-Ref.kanal: -

Figure 3.9: GUI of the Müller-BBM PAK software and FFT parameters used.

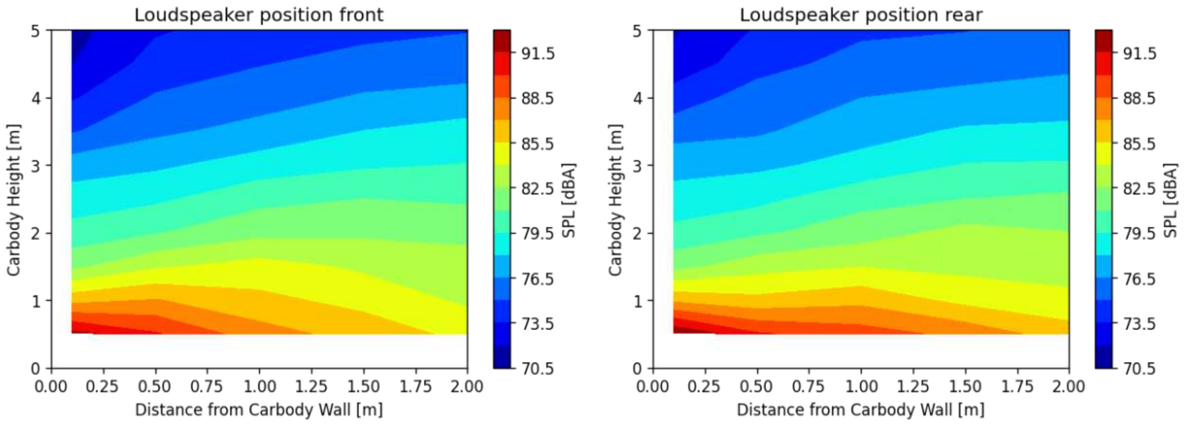

(a) Loudspeaker position front

(b) Loudspeaker position rear

Figure 3.10: Pressure field around car body.

In Fig. 3.10, a visualization of the total pressure field around the carbody is shown. The horizontal axis represents the distance from carbody wall, the vertical axis the height above ground and the color the overall A-weighted pressure level, respectively. The white space in the plot is due to the missing data in the measurement since the measurement positions start at 10 cm away from carbody wall and half meter above ground. Comparing the pressure field of the two different loudspeaker locations, the asymmetric effect introduced by the brake disc can be observed. The brake disc of the front wheel axle standing in the transmission path of the loudspeaker seems to block a part of the acoustic wave.

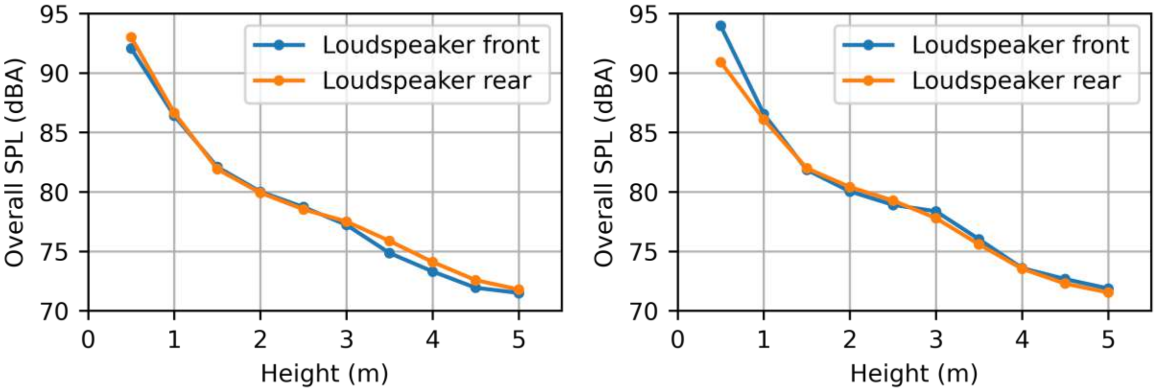

(a) Measurement position a

(b) Measurement position c

Figure 3.11: Overall A-weighted sound pressure level at example measurement positions.

In order to compare the pressure field quantitatively, one can plot the acoustic pressure as function of height for different measurement positions, which can be seen in the figures above. In 3.11a it can be observed that at measurement position a, the pressure curve caused by loudspeaker at different locations shares similar shape, and the pressure is strictly decreasing over carbody height.

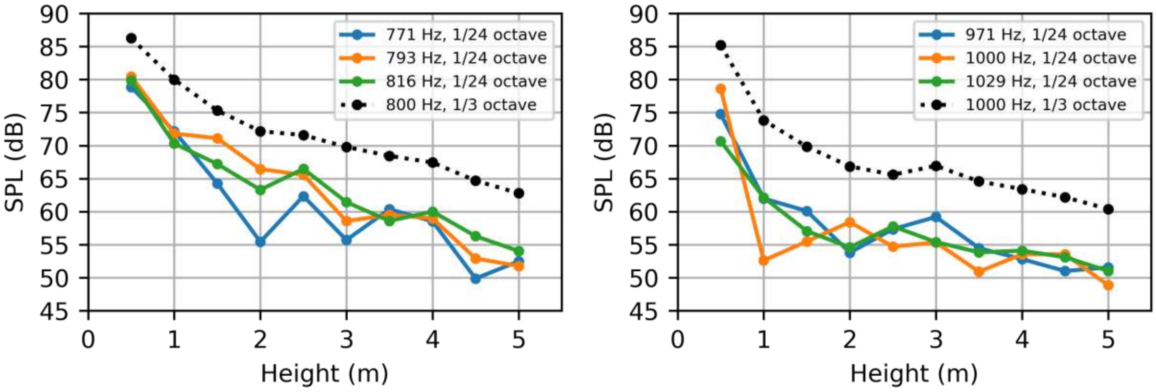

(a) 800 Hz

(b) 1000 Hz

Figure 3.12: SPL distribution of example third octave bands at measurement position a with loudspeaker at the rear. Solid line: 1/24-octave center frequency. Dashed line: 1/3-octave center frequency.

In Fig. 3.12, the sound pressure level over height for different 1/n octave band center frequencies is displayed. In the 1/24 octave resolution, several local minima in the curve shape can be observed, e.g., for 771 Hz in fig. 3.12a or for 1000 Hz in Fig. 3.12b, which are caused by the destructive interference of the acoustic wave. The destructive interference can also be observed in the pressure field of the single frequency band as shown in Fig. 3.13, sinks in acoustic field are to be found at about 1 m and 3.5 m height, respectively, which correspond to the position of the local minima in Fig. 3.12b.

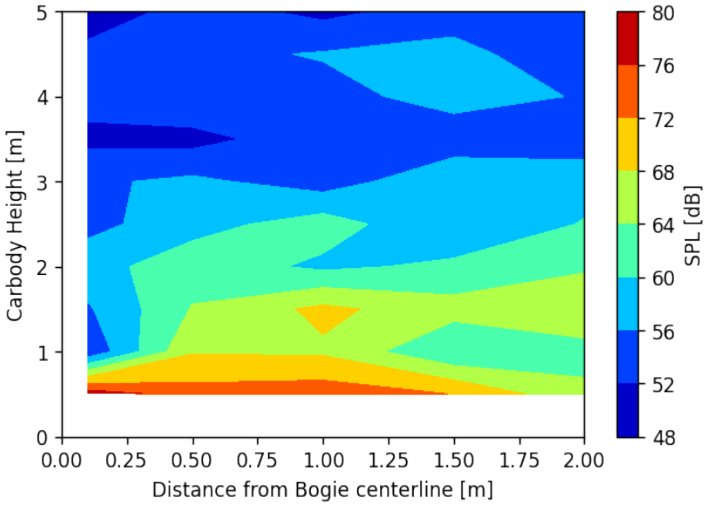

Figure 3.13: Pressure field of 1/24-octave frequency 1000 Hz with loudspeaker placed at the rear.

Chapter 4

Finite Element Modeling

This chapter outlines the development of the finite element model of the X-Wagen metro and the simulation setup. First, in Section 4.1, the design of the model geometry and the mesh of the computational model are shown. Subsequently, Section 4.2 describes the incorporation of boundary conditions into the finite element model and the modeling approach of the loudspeaker sound source. Finally, in Section 4.3, a parametric study is carried out to investigate the influence of different simulation parameters on the solution of the initial finite element model. All these simulations are executed with the acoustics module of the open-source FEM software openCFS [29].

4.1 Geometry and mesh

Due to the large dimension of the vehicle (about 19 m long per metro car), a simulation of the complete metro train would be too extensive from the computational point of view. Hence, the modeling domain has to be confined to a selected section of the car, which surrounds the front non-driven bogie at the head car of the metro. The considered region has been marked through a red box in Fig. 4.1. Furthermore, the outer pressure field measurement described in Section 3.2 has been taken in the same area.

The geometry of the modeled car section consists of the car body shell and the non-driven bogie. The dimension parameters of the modeled components are measured from the 3D model of the X-Wagen (see Fig. 2.4 and Fig. 2.6). As described in Section 2.4, if the brake disc and the brake caliper are disregarded, the symmetry of the bogie can be exploited. Furthermore, due to the symmetry of the car body shell in its width and length direction, only one-fourth of the car section is modeled in order to reduce computational effort. The quarter model of the car section is depicted in Figure 4.2a, whereas the equivalent model, namely the full model, is shown in Fig. 4.2b. Both models are shown for a more comprehensive illustration of the model geometry, but only the quarter model has been used in the simulation. For simplification of the geometry design, only the most essential components have been included in the model. As shown in Figure 4.2a, the contemplated components are the squared car body shell (dark green), the bogie frame (purple), the wheel with axle (pink) and the air suspension (gray). The omnidirectional loudspeaker

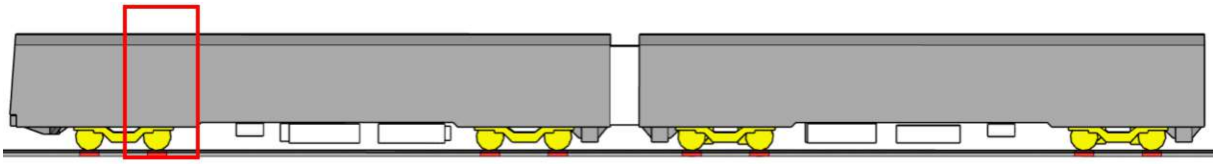

Figure 4.1: Side view of the X-Wagen 3D model, where the red box indicates the modeling area.

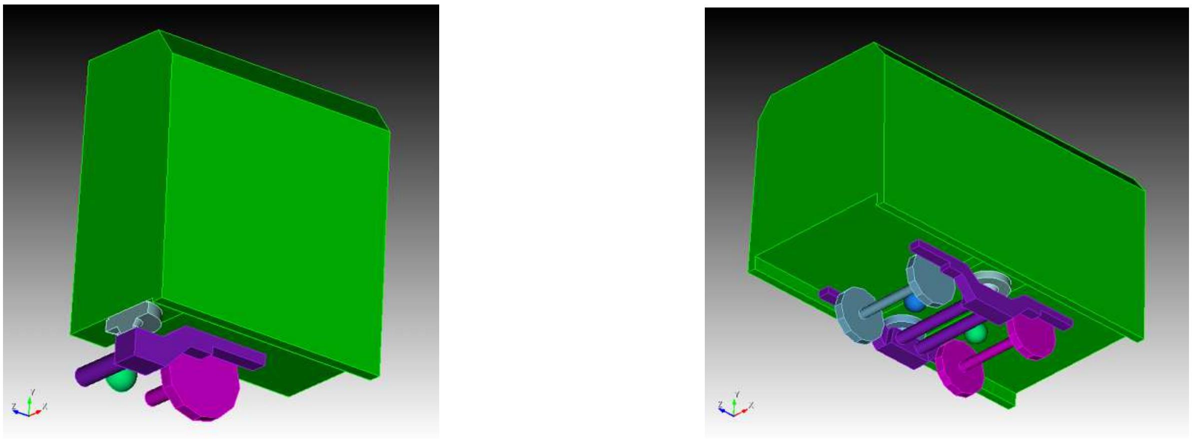

(a) One-fourth model.

(b) Full model.

Figure 4.2: Geometry of the modeled car section. The full model is shown for better illustration. The one-fourth model has been used for the simulation.

(bright green) is represented through a sphere with 35 cm and is placed at the exact same position as in the validation measurement (see Fig. 3.6).

After the car section geometry is designed, the actual computational model (see Fig. 4.3) used for the acoustic simulation is obtained by cutting the car section model out of an acoustic fluid (in this case, air) volume. Likewise, only one-fourth of the volume is considered due to the symmetry of the problem. Since the radiation of the underfloor noise into the free field around the vehicle is of interest, the acoustic region is surrounded by a perfectly matched layer (Ω_{PML}) to model the open domain. To reduce the effort of the meshing process of the model geometry, the propagation region is divided into two sub-regions, namely the region that surrounds the bogie components (Ω_1) and the main propagation region (Ω_2), respectively. The main propagation region has the same length as the one-fourth car section model of 2.6 m and a height of 4.52 m so that the upper boundary of the acoustic region is about 1 m above the car roof. The choice of the propagation domain width needs to be well considered. While using an insufficient domain width, i.e., with the PML being placed very close to the acoustic source, might cause nonphysical behavior of the acoustic wave in the thin region between the vertical carbody wall and the PML. Setting the domain width too large would increase the computational effort of the simulation extensively. According to several PML usage guidelines [30–32], a minimum distance of half of the simulation frequency wavelength ($\lambda/2$) to the radiating source is recommended. This criteria is fulfilled for the domain height (4.52 m) and the length (2.6 m) using the lowest simulation frequency of 100 Hz ($\lambda/2 = 1.71$ m). The actual domain width used for the simulation will be determined in a later parameter study.

Subsequently, a mesh of the model geometry (see Fig. 4.4) was created using the mesh generator Coreform Cubit [33], which offers several advanced semi-automatic meshing techniques that can extensively lower the effort of the meshing process. The sub-region Ω_1 contains complex outlines of the bogie components, and is therefore meshed using tetrahedral elements, which are perfectly suitable for meshing complex geometries but are more computationally expensive than the hexahedral elements at comparable solution accuracy. To lower the computational cost of the model, the main propagation region Ω_2 is meshed using hexahedral elements. For both regions, second-order (quadratic) element type is used (p-refinement) to reduce discretization errors, which is computationally more efficient than using a smaller element size (h-refinement) [34]. Special care needs to be taken if a hextet mesh combination is used. Thereby, the sub-regions Ω_1 and Ω_2 are coupled by non-conforming interfaces Γ_{NC}, which allow different element types and sizes to be used in the same mesh. For the simulation, the default setup of

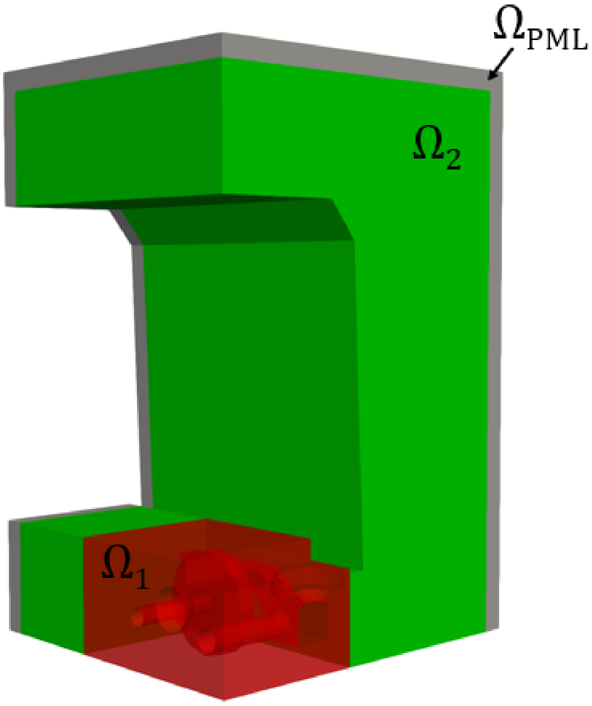

Figure 4.3: Computational model consists of an acoustic fluid (air) volume surrounded by a PML domain (Ω_{PML}). The acoustic domain is divided into two sub-regions Ω_1 and Ω_2 for an easier meshing of the geometry. Thereby, Ω_1 is displayed semi-transparently to illustrate the outlines of the bogie components.

the non-conforming interface in openCFS is used, if which of the Nitsche type. For detailed information of non-conforming interfaces, one can refer to, e.g., Kaltenbacher et al. [35]. For the PML region Ω_{PML}, Kaltenbacher [22] recommended using a least four linear elements and two quadratic elements in the PML thickness direction and using the same spatial discretization as of the acoustic domain. For the sake of enhancing the stability of the performance of the PML, three quadratic hexahedral elements are used in the mesh of the finite element model. The damping function used in the PML region is the inverse distance damping (see Eq. (2.36)), which is the default option in openCFS. Through a preliminary study of the problem, the frequency analysis range of the simulation is set to 100 Hz to 2000 Hz in one-third octave bands, resulting in 14 frequency bands in the given range, shown in Tab. 4.2. As can be read from the table, the lower and the upper limits of the frequency analysis are 89 Hz and 2262 Hz, respectively. Due to the broad range of the analyzed frequencies, using a constant mesh size covering the entire range would be challenging. On the one hand, using a mesh size corresponding to the highest simulation frequency for all frequencies would be computationally too expensive; on the other hand, using a mesh size that is designed for lower frequency bands would increase discretization errors in higher frequency bands, since the wavelength would be resolved insufficiently. The solution to this problem is to choose a mesh discretization depending on the analysis frequency band. For the finite element simulation of the X-Wagen, four different grids as shown in Tab. 4.3 are prepared. The discretization size is chosen so that the wavelength corresponding to the upper cutoff frequency of the analyzed one-third octave band is resolved by at least six elements, i.e., $h = \lambda_{f_u}/6$, which also means for any lower frequencies, the discretization is getting finer (with respect to the wavelength). The bogie components contain complex and, more importantly, small surfaces that require a fine discretization of the surface mesh, which is not fulfilled for low frequency bands like, e.g., 100 Hz ($\lambda_{100\,\text{Hz}}/6 = 0.57\,\text{m}$). It has been shown that using a discretization size corresponding to the wavelength of 1000 Hz ($\text{h} = 0.057\,\text{m}$) could mesh the surfaces adequately. Hence, this grid size is used for the one-third octave bands from 100 Hz to 800 Hz. Since the

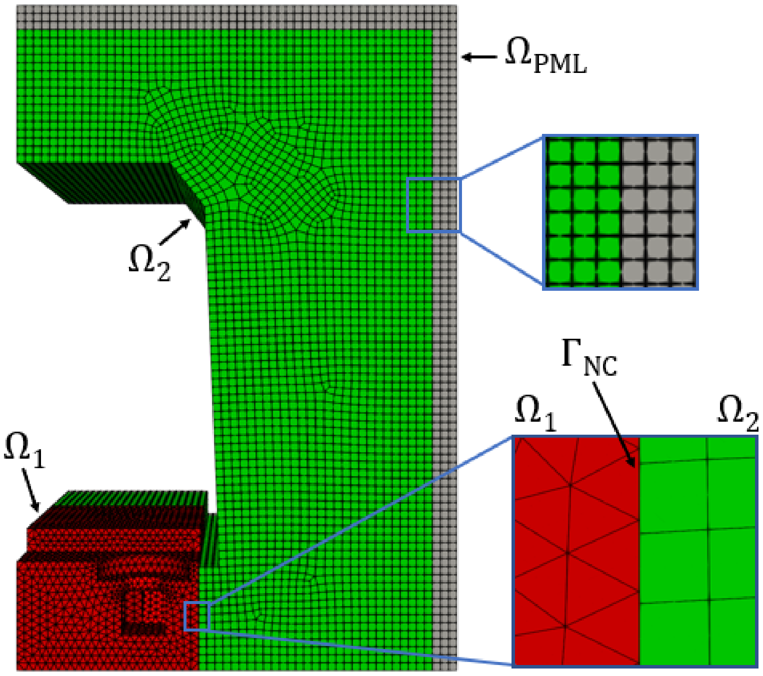

Figure 4.4: Mesh of the computational model. The acoustic sub-regions Ω_1 and Ω_2 are meshed with tetrahedral and hexahedral elements, respectively. Both sub-regions are coupled with non-conforming interfaces Γ_{NC} of Nitsche type. For the PML region Ω_{PML}, a constant number of three quadratic hexahedral elements along the thickness direction are used. All regions Ω_1, Ω_2, Ω_{PML} share the same maximum element size, which is frequency-dependent, as shown in Tab. 4.3.

upper frequency limit of the 1000 Hz band is greater than 1000 Hz, a finer grid size would be necessary so that the mentioned discretization criteria still hold. Hence, the 1000 Hz band and the 1250 Hz band share the same grid size of 0.036 m. For the highest frequency bands 1600 Hz and 2000 Hz, respectively, individual grid sizes are used. The above-mentioned parameters of the mesh of the finite element model as well as the material parameters used for the acoustic domain are summarized in Tab. 4.1.

Variation of the simulation domain width

The aim of this parameter study is to find an appropriate simulation domain size that provides sufficient numerical accuracy while keeping the computational effort of the simulation in an adequate range. Thereby, the length and the height of the main propagation region Ω_2 are kept constant while varying only the width of the domain. In what follows, the domain width is defined as the distance between the lower edge of the car body wall and the outer boundary of the main propagation region Ω_2, as depicted in Fig. 4.5b. For the parameter study, 5 different domain widths are used, which are 0.2 m, 0.5 m, 1 m, 1.5 m and 2 m, respectively. The model with the smallest and the largest width are shown in Fig. 4.5, respectively. According to several PML usage guidelines [30–32], placing the PML at a distance of half of the wavelength to the radiating source would be sufficient for most of the cases. For our simulation, it would be 1.71 m, which is the half of the wavelength corresponding to the lowest analysis frequency 100 Hz. Hence, the reference solution is computed by using the model with 2 m width and all errors are evaluated with respect to this reference. For the simulation, a fictitious excitation with uniform normal surface particle velocity of $u_s = 1\,\mathrm{mm}\cdot\mathrm{s}^{-1}$ is applied to the loudspeaker surface. The acoustic pressure is evaluated at 0.1 m away from the vehicle along the height direction as indicated by the vertical red lines in Fig. 4.5a and Fig. 4.5b. Along the height direction, the evaluation points of the acoustic pressure

Table 4.1: Parameters of the computational model.

Propagation region	
Element type Ω_1	quadratic tetrahedral element
Element type Ω_2	quadratic hexahedral element
Maximum element size Ω_1, Ω_2	frequency-dependent, see Tab. 4.3
PML region	
Number of elements along thickness direction	3
Element type	quadratic hexahedral element
Element size	same as Ω_1, Ω_2
Damping function type	inverse distance damping, see Eq. (2.36)
Non-conforming interface	
Master domain	Ω_1
Slave domain	Ω_2
Type of mortaring	Nitsche (OpenCFS default)
Penalization-parameter	100 (OpenCFS default)
Material (air at 20 °C)	
Density ρ_0	$1.204\,\mathrm{kg \cdot m^{-3}}$
Bulk modulus K	$142\,\mathrm{kPa}$
Speed of sound c_0	$343.21\,\mathrm{m \cdot s^{-1}}$
Characteristic acoustic impedance Z_0	$413.3\,\mathrm{Pa \cdot s \cdot m^{-1}}$

Table 4.2: One-third octave bands used for the simulation. The quantities f_c, f_l, f_u denote the center frequency, the lower cutoff frequency and the upper cutoff frequency of the corresponding frequency band, respectively.

Band	f_c (Hz)	f_l - f_u (Hz)
1	100	89 - 112
2	125	112 - 141
3	160	141 - 178
4	200	178 - 224
5	250	224 - 283
6	315	283 - 356
7	400	356 - 449
8	500	449 - 565
9	630	565 - 713
10	800	713 - 897
11	1000	897 - 1131
12	1250	1131 - 1425
13	1600	1425 - 1796
14	2000	1796 - 2262

Table 4.3: Frequency-dependent discretization size of computational grids.

	Used for one-third octave bands (Hz)	Discretization size h (m)
Grid 1	100, 125, 160, 200, 250, 315, 400, 500, 630, 800	0.057
Grid 2	1000, 1250	0.036
Grid 3	1600	0.029
Grid 4	2000	0.025

are 0.05 m from each other, starting from 0 m and ending with 4.5 m, resulting in 91 evaluation positions in total. At each evaluation point, the relative error of the acoustic pressure value $\hat{p}_{a,i}$ (real part and imaginary part) to the reference solution $\hat{p}_{a,\mathrm{ref},i}$ is computed by

$$E_{p_a,i} = \frac{\left|\hat{p}_{a,i} - \hat{p}_{a,\mathrm{ref},i}\right|}{\left|\hat{p}_{a,\mathrm{ref},i}\right|}\,, \tag{4.1}$$

with i being the evaluation position and $i \in [1 \ldots 91]$. The simulation is carried out with the one-third octave center frequencies from 100 Hz to 2000 Hz, using the computational grids as displayed in Tab. 4.3.

The relative error $E_{p_a,i}$ along the domain height direction using different domain widths for frequency 100 Hz and 2000 Hz are shown in Fig. 4.6. As can be seen for both frequencies, the smallest domain width has the largest error among all domain widths, and the magnitude of the relative error decreases with increasing domain width. For the same domain width, the relative error depends on the evaluation points and increases with the height, which is due to a decreasing width to height ratio. It can be seen that although the smallest domain width 0.2 m has a quite large relative error in the higher area (up from 2 m), for the area below 1 m, it has a similar level of error as the larger domain. This means that if only the acoustic pressure at the lower area, for example in the underfloor area of the metro, is of interest, the domain boundary can be set very close to the carbody, reducing the computational effort extensively. The same behavior of the relative error has also been shown for other frequencies.

To find a suitable domain width for our finite element model, the maximum relative error $E_{p_a,\mathrm{max}}$ and the average relative error $E_{p_a,\mathrm{max}}$ over all 91 evaluation positions are computed for each one-third octave center frequency. The obtained results are shown in Fig. 4.7; additionally, the concrete values are summarized in Tab. 4.4. As can be seen from the results, both maximum error and average error decrease with increasing domain width. Up from the domain width of 1 m, the maximum relative error among all frequencies is limited by 10 %, and in terms of the average error, the error is limited by 1.5 %. Setting a average error limit to 2 %, which corresponds to a deviation of 0.17 dB in the sound pressure level, choosing 1 m to be the domain width of our finite element model would be adequate when considering the rising computational effort using a larger domain width. It has been shown by the simulation that the computational effort using the coarsest grid (Grid 1) with 1.5 m domain width is still in a good range. Hence, for the computational grid for lower frequency bands (100 Hz to 800 Hz) a domain width of 1.5 m is used to further increase the numerical accuracy of the model.

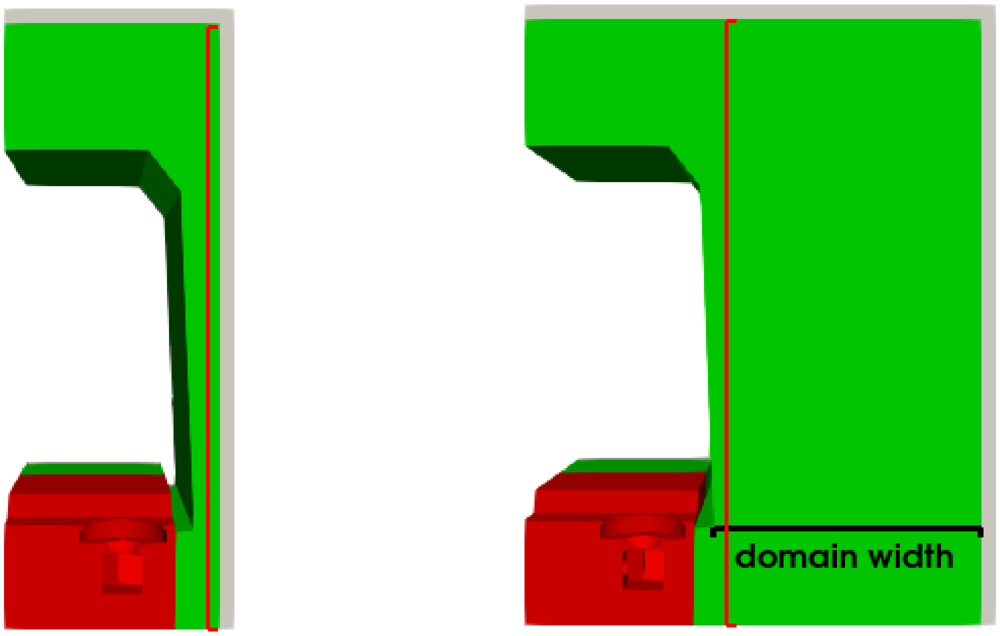

(a) 0.2 m

(b) 2 m

Figure 4.5: Computational models with different propagation domain widths, which are defined as the distance between lower edge of the car body wall and the region outer boundary. The vertical red lines indicate the evaluation position of the acoustic pressure, which is at 10 cm away from the lower car body edge.

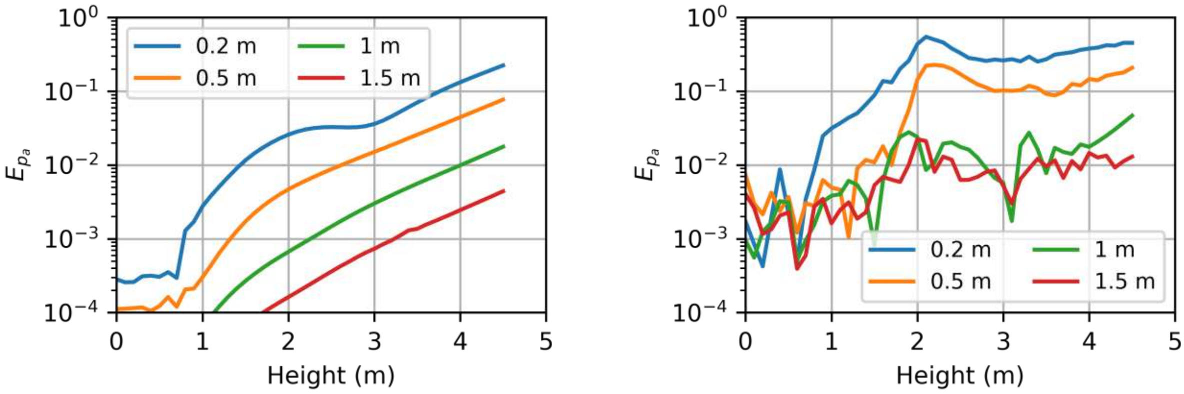

(a) 100 Hz

(b) 2000 Hz

Figure 4.6: Relative error E_{p_a} over the domain height for frequency 100 Hz and 2000 Hz.

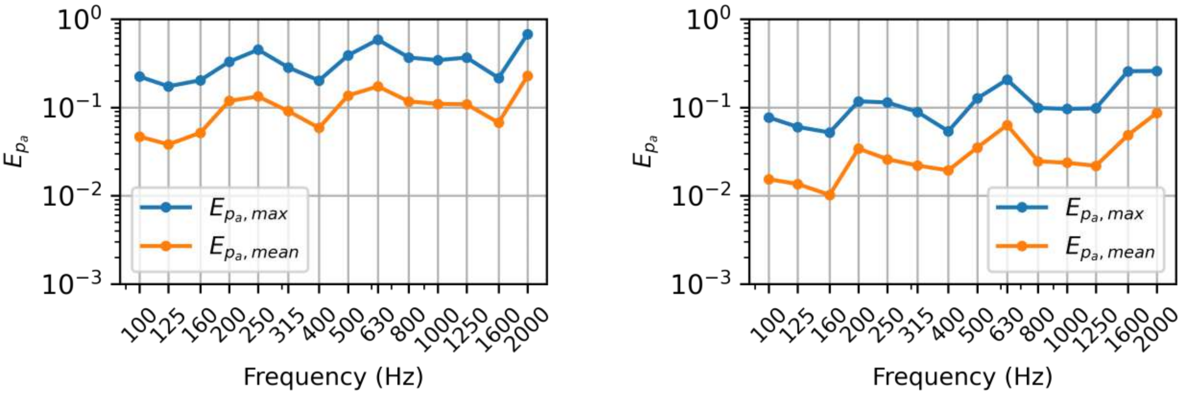

(a) 0.2 m

(b) 0.5 m

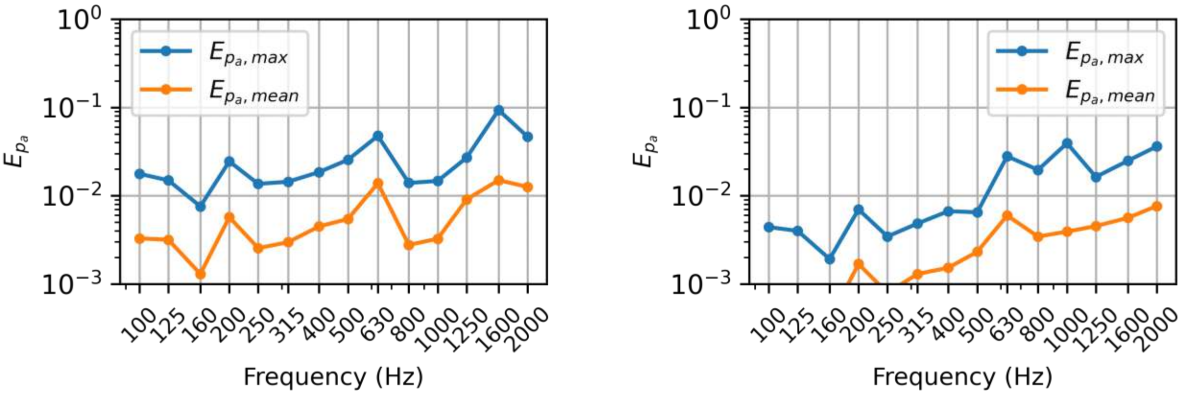

(c) 1 m

(d) 1.5 m

Figure 4.7: The maximum relative error $E_{p_a,\max}$ and the mean relative error $E_{p_a,\text{mean}}$ of one-third octave center frequencies for different domain widths.

Table 4.4: Computed errors (in %) in the acoustic pressure for different domain widths.

	0.2 m		0.5 m		1 m		1.5 m	
Frequency (Hz)	$E_{p_a,\max}$	$E_{p_a,\text{mean}}$	$E_{p_a,\max}$	$E_{p_a,\text{mean}}$	$E_{p_a,\max}$	$E_{p_a,\text{mean}}$	$E_{p_a,\max}$	$E_{p_a,\text{mean}}$
100	22.40	4.67	7.72	1.54	1.77	0.33	0.44	0.08
125	17.36	3.81	6.02	1.36	1.49	0.32	0.40	0.08
160	20.35	5.17	5.21	1.02	0.76	0.13	0.19	0.04
200	33.01	11.89	11.73	3.42	2.45	0.57	0.70	0.17
250	45.14	13.32	11.40	2.59	1.36	0.25	0.34	0.08
315	28.48	9.11	8.91	2.20	1.44	0.30	0.48	0.13
400	20.19	5.87	5.38	1.93	1.85	0.45	0.67	0.15
500	38.88	13.65	12.67	3.51	2.55	0.54	0.65	0.23
630	58.67	17.33	20.67	6.31	4.77	1.38	2.80	0.60
800	36.81	11.71	9.89	2.46	1.39	0.28	1.96	0.34
1000	34.36	10.98	9.63	2.36	1.47	0.33	3.94	0.39
1250	36.77	10.86	9.79	2.18	2.70	0.91	1.63	0.45
1600	21.59	6.71	25.76	4.85	9.34	1.50	2.49	0.56
2000	67.73	22.74	25.95	8.66	4.67	1.26	3.62	0.76

Computational effort of the finite element model

During the domain width parameter study, the computational effort of the finite element model used for the acoustic simulation of the X-Wagen was also evaluated. In the final model setup, a domain width of 1.5 m is applied to the computational grid for frequency bands 100 Hz to 800 Hz, while the other grids for higher frequency bands have a domain width of 1 m. In the simulation setup, each frequency band is resolved by 9 intermediate frequencies, i.e., nine harmonic steps have to be computed per analyzed one-third octave band. In this thesis, all computations were performed on the Sessanta server of the Institute of Mechanics and Mechatronics of TU Wien, which is equipped with 1 Terabyte RAM and two AMD EPYC 7542 32-core processors. The simulations were run with openCFS using 32 physical cores and the obtained computational efforts of the final design of the finite element model are listed in Tab. 4.5. As can be read from the results, the computational effort of the model consisting of the required memory the computation time increase with the total unknowns, i.e., nodes in the computational grid. While the computation time for the coarsest grid is only half an hour, the highest frequency band needs almost 24-fold the time to compute. The total computation time of the model is calculated as $10 \times 0.5\,\mathrm{h} + 2 \times 2\,\mathrm{h} + 5.5\,\mathrm{h} + 12\,\mathrm{h} = 24.5\,\mathrm{h}$. One can see that almost half of the total computation time was spent on the computation of the highest frequency band. The total computation time was obtained by running the simulation jobs sequentially; the actual computation time can be shortened if the jobs are executed in parallel. If the computation time is not considered, the upper limit of the frequency band that can be analyzed is restricted by the required memory, since this rises with the degrees of freedom in the computational mesh. In a three-dimensional acoustic problem, a doubling of the analyzed frequency while keeping the same discretization size would leads to an eight times larger number of degrees of freedom in the system, since the number of elements is also doubled in each spatial direction. That means that with a given amount of the memory, the size of the acoustic domain needs to be more confined if an analysis using higher frequency bands is of interest. For our finite element model, the required memory for the highest frequency band is about 260 GB, without making the acoustic domain much smaller, it is not possible to increase the frequency range of interest.

Table 4.5: Computational effort of the final model.

	Domain width	Total unknowns	Required RAM	Solution time (9 harmonic steps)
Grid 1	1.5 m	0.8 million	20 GB	0.5 hours
Grid 2	1 m	2.3 million	70 GB	2 hours
Grid 3	1 m	4.4 million	150 GB	5.5 hours
Grid 4	1 m	6.6 million	260 GB	12 hours

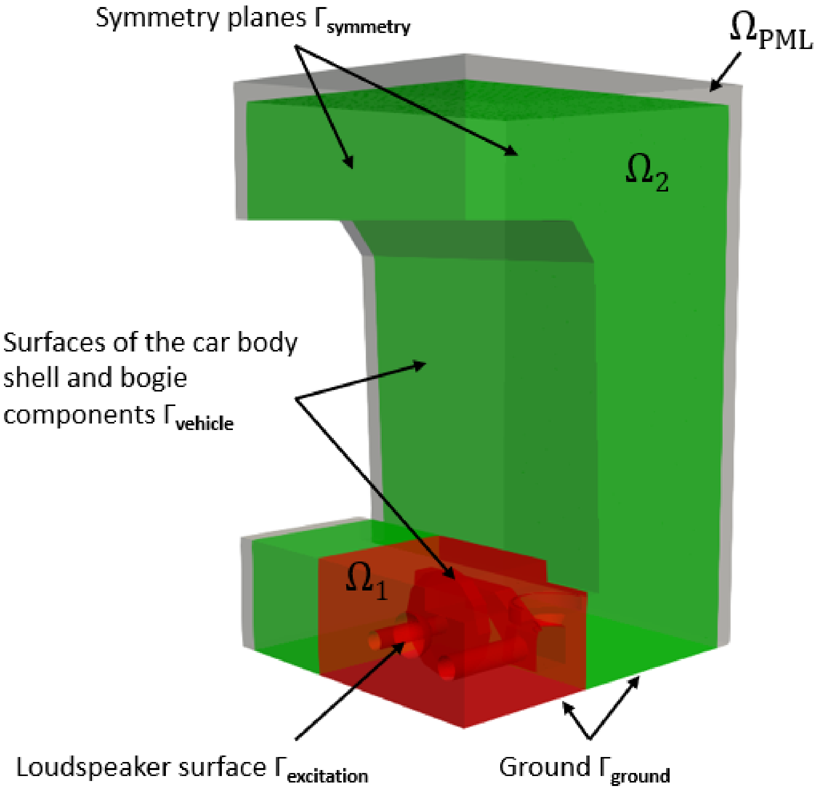

Figure 4.8: Boundary surfaces of the finite element model.

4.2 Boundary conditions and loads

After the consideration of the geometrical model in the previous section, the physical modeling aspects will be now discussed. In the finite element model of the X-Wagen, two boundary conditions of Neumann type are used: the sound hard (homogeneous) boundary condition and the normal velocity (inhomogeneous) boundary condition. The boundary surfaces of the model are shown in Fig. 4.8. The concrete ground Γ_{ground} and the wrapped surfaces of the car body shell and the bogie components Γ_{vehicle} are assumed to be fully reflective. This also applies to the both symmetry planes (X-Y and Z-Y plane) of the quarter model Γ_{symmetry}. Hence, the sound hard boundary condition is used for these surfaces

$$\nabla p_a \cdot \boldsymbol{n} = 0 \qquad \text{on} \qquad \Gamma_{\text{ground}} \cup \Gamma_{\text{vehicle}} \cup \Gamma_{\text{symmetry}} \,. \tag{4.2}$$

The acoustic excitation of the computational model comes from the loudspeaker, for which a normal velocity boundary condition is defined on its surface $\Gamma_{\text{excitation}}$, which reads as

$$\boldsymbol{u_a} \cdot \boldsymbol{n} = u_n \qquad \text{on} \qquad \Gamma_{\text{excitation}} \,. \tag{4.3}$$

However, the sound source characterization measurement from Section 3.1 results in a acoustic power spectrum that cannot be directly applied to the finite element model. Therefore, a modeling approach of the sound source has to be found that can relate the surface normal velocity with the acoustic power.

Modeling of the sound source

In the following, the modeling approach of the sound source is explained. Thereby, the loudspeaker sound source is modeled as a pulsating sphere radiating into free field, which is excited by a prescribed surface normal velocity with amplitude $\hat{u}_s = \hat{u}_a(a)$ with a being the radius of the sphere. The pressure amplitude of the spherical wave at a distance r from the sound source is given by

$$\hat{p}_a(r) = \frac{\hat{A}}{r}\, e^{-jkr}\,, \tag{4.4}$$

with $\hat{A}$ being the monopole amplitude and k being the wave number of the propagating wave. The relationship between the pressure amplitude and the amplitude of the particle velocity is described by the specific acoustic impedance, which for spherical wave computes by

$$Z(r) = \frac{\hat{p}_a(r)}{\hat{u}_a(r)} = \rho_0 c_0 \frac{jkr}{1+jkr}\,, \tag{4.5}$$

where ρ_0 is the density of the propagation medium and c_0 is the speed of sound in the medium. The product $Z_0 = \rho_0 c_0$ is also called the characteristic impedance of the propagation medium. The particle velocity of the spherical wave can then be expressed by

$$\hat{u}_a(r) = \frac{\hat{p}_a(r)}{Z(r)} = \frac{\hat{A}}{rZ_0}\, e^{-jkr}\left(1 + \frac{1}{jkr}\right)\,. \tag{4.6}$$

For stationary sound field, the average power density or the sound intensity is given by

$$I(r) = \frac{1}{2}\mathrm{Re}\{\hat{p}_a(r)\hat{u}_a^*(r)\}\,, \tag{4.7}$$

where $()^*$ denotes the complex conjugate. By inserting Eq. (4.4) and Eq. (4.6) into the expression of the sound intensity, one obtains

$$\begin{aligned} I(r) &= \frac{1}{2}\mathrm{Re}\{\frac{\hat{A}\hat{A}^*}{r^2 Z_0}\, e^{-jkr}\, e^{jkr}\left(1 + j\frac{1}{kr}\right)\} \\ &= \frac{1}{2}\frac{|\hat{A}|^2}{r^2 Z_0}\,. \end{aligned} \tag{4.8}$$

Furthermore, the acoustic power W of a steady sound source radiating into free field is obtained by integrating the sound intensity $I(r)$ over a surface Γ enclosing the sound source and can be found as

$$W = \oint_\Gamma I(r)\,\mathrm{d}\Gamma = \bar{I}(r)\,4\pi r^2 = \frac{2\pi|\hat{A}|^2}{Z_0}\,. \tag{4.9}$$

As apparent in Eq. (4.9), the acoustic power is independent from the distance to the sound source and can be related to the monopole amplitude $\hat{A}$. Assume a sound source has a radius of a, the pressure amplitude on the sound source surface $\hat{p}_s = \hat{p}_a(a)$ can be expressed by the product of the surface normal velocity $\hat{u}_s = \hat{u}_a(a)$ and the specific impedance $Z(a)$ evaluated at the source surface and is found by

$$\hat{p}_s = \hat{p}(a) = \hat{u}_s Z(a) = \frac{\hat{A}}{a}\, e^{-jka}\,. \tag{4.10}$$

Upon bringing the monopole amplitude $\hat{A}$ to one side of the equation, and evaluating Eq. (4.5) at the source radius a, one obtains

$$\hat{A} = a\hat{u}_s Z(a)\, e^{jka} \tag{4.11}$$

$$= a\hat{u}_s Z_0 \frac{jka}{1+jka}\, e^{jka}\,. \tag{4.12}$$

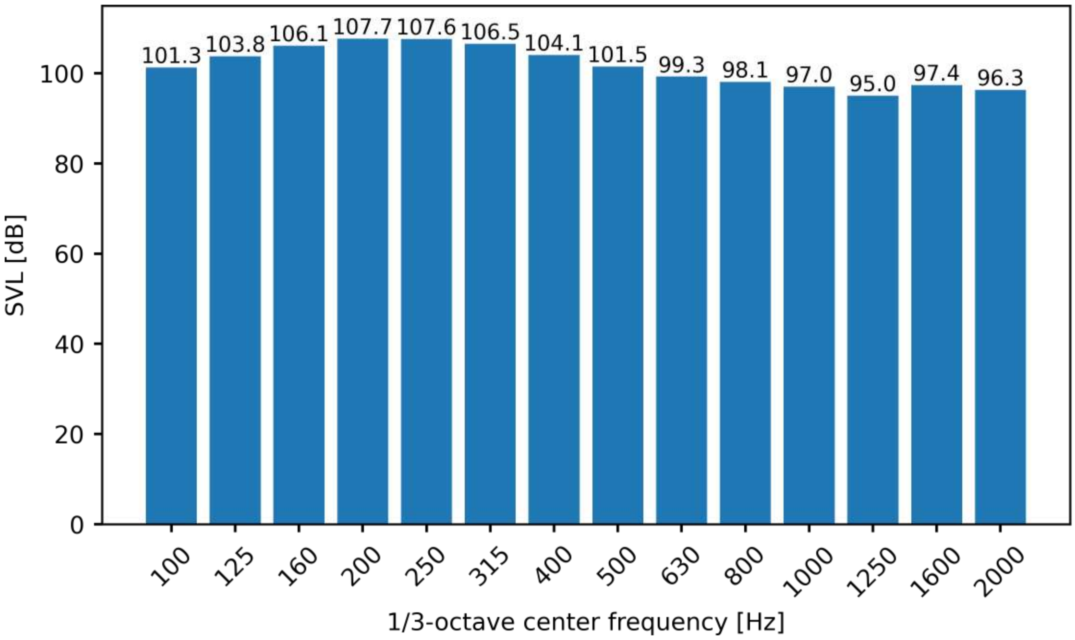

Figure 4.9: SVL spectrum of the surface normal velocity in dB ref. $5 \cdot 10^{-8}$ m/s, calculated from the measured acoustic power spectrum (Fig. 3.4c) using Eq. (4.14).

By inserting Eq. (4.12) into Eq. (4.9), the acoustic power W can hence be expressed by the surface normal velocity $\hat{u}_s$, which reads as

$$W = 2\pi a^2 Z_0 \left|\hat{u}_s\right|^2 \frac{(ka)^2}{1+(ka)^2} \, . \tag{4.13}$$

Assuming that the surface normal velocity is real-valued only, i.e., $|\hat{u}_s| = \hat{u}_s$, one obtains

$$\hat{u}_s = \sqrt{\frac{W(1+k^2a^2)}{2\pi Z_0 k^2 a^4}} \, . \tag{4.14}$$

Through Eq. (4.14), the required normal velocity at the loudspeaker surface $\Gamma_{\text{excitation}}$ for a given acoustic power can be calculated. Therefore, the measured acoustic power spectrum of the sound source (see Fig. 3.4c) can be converted into a surface normal velocity spectrum, which is shown in Fig. 4.9.

Note that above derivation is only valid for the assumption of free-field radiation of the spherical wave. It aims to find a possible way to incorporate the measured acoustic power into the finite element model. For a general radiation domain, specifying a normal velocity boundary condition on a sphere surface does not guarantee a certain acoustic power as measured in the free field, since the resulting pressure is dependent on the specific acoustic impedance, and the latter depends on the acoustic system.

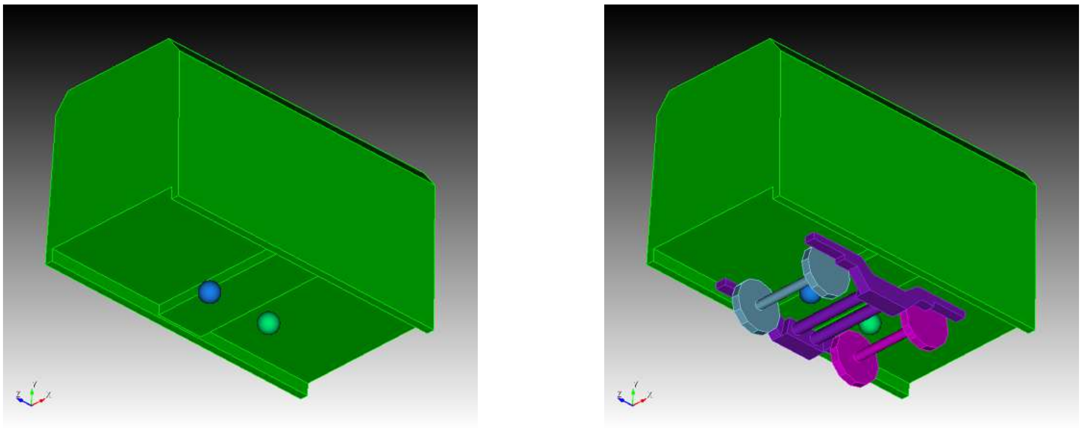

(a) No underfloor components (b) No air suspension

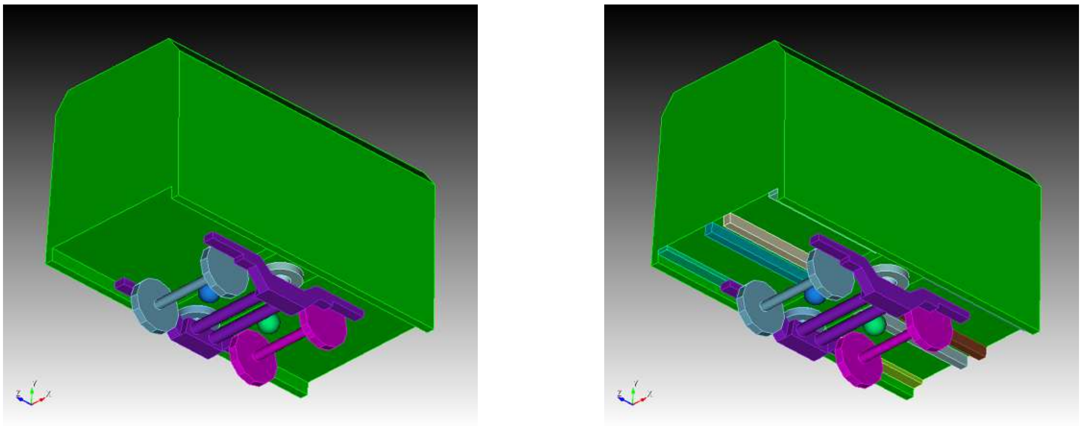

(c) Initial model (d) Additional structures

Figure 4.10: Underfloor geometry with four variations.

4.3 Parametric study

4.3.1 Variation of underfloor geometry

In the initial geometric setup, the contemplated underfloor components in the finite element model are the bogie frame, the wheel with axle, and the air suspension. In order to investigate the stability of simulation results to different underfloor geometrical setups, a parametric study with a variation of the underfloor geometry is carried out in the following.

For the parametric study, four different variations of underfloor geometry including the initial finite element model as described in Section 4.1 are prepared, which are shown in Fig. 4.10, ordered by their complexity. Again, the full model of each geometry is shown for a better illustration, whereby the one-fourth model will be used for the simulation. The simplest model (Fig. 4.10a) contains only the carbody shell without any underfloor components; the blue or the green sphere beneath the car floor represents the omnidirectional loudspeaker. In the next, more complex model (Fig. 4.10b), the bogie frame and the wheels are considered, and it differs from the initial geometry (Fig. 4.10c) only by the air suspension. Therefore, this variation is also named "no air suspension". Finally, the last geometrical model (Fig. 4.10d) is set up by attaching additional structures to the car floor, which represent the cable ducts beneath the car floor.

4.3.2 Variation of ground surface impedance

In the initial simulation setup, the ground is modeled as a fully reflective surface at which the homogeneous Neumann (sound hard) boundary condition is applied. However, it is also of interest to investigate the influence of including ground absorption on the simulation result. An absorbing surface is characterized by its absorption coefficient α, which is frequency dependent in most cases. In the finite element formulation, the reflection and absorption of the incident acoustic wave at a surface is described by the surface impedance boundary condition, which can be related to the absorption coefficient of the surface. In the following, the relation between the absorption coefficient α and the surface impedance Z_s is presented following Nedkov [36].

The sound absorption coefficient α of a material is defined by the ratio of the absorbed acoustic power W_{absorbed} and the power of incident wave W_{incident}, which for wave at normal incidence reads as

$$\alpha = \frac{W_{\text{absorbed}}}{W_{\text{incident}}} = 1 - |R|^2 \,, \tag{4.15}$$

with R being the complex reflection coefficient, which can be represented as

$$R = \frac{Z_s - Z_0}{Z_s + Z_0} = \frac{\frac{Z_s}{Z_0} - 1}{\frac{Z_s}{Z_0} + 1} \,, \tag{4.16}$$

where $Z_0 = \rho_0 c_0$ is the characteristic impedance of the propagation medium and Z_s is the specific acoustic impedance of the absorbing surface. The impedance ratio $\frac{Z_s}{Z_0}$ is also called the normalized surface impedance

$$\tilde{Z}_s = \frac{Z_s}{Z_0} = \tilde{R}_s + j\tilde{X}_s \,, \tag{4.17}$$

which can be slit into a real part $\tilde{R}_s$ and an imaginary part $\tilde{X}_s$. By inserting Eq. (4.16) into Eq. (4.15), the absorption coefficient α can be related to the complex surface impedance by

$$\alpha = \frac{4\tilde{R}_s}{\tilde{R}_s^{\,2} + \tilde{X}_s^{\,2} + 2\tilde{R}_s + 1} \,. \tag{4.18}$$

In order to uniquely define the surface impedance $\tilde{Z}_s$ of the absorbing surface for a given normal incident absorption coefficient α, the phase of the complex surface impedance also has to be known, which is given by

$$\varphi = \arctan \frac{\tilde{X}_s}{\tilde{R}_s} \,. \tag{4.19}$$

The impedance characteristic of a ground surface can be determined for example by an in-situ measurement using impedance tube method [6,37]. In cases where a measurement is not accessible, the absorption data can be retrieved, e.g., from a acoustic data bank, which, in most cases, provides only the absorption coefficient spectrum instead of the complex surface impedance. However, it has been shown that also the phase has to be provided to uniquely define the surface impedance for a given absorption coefficient. In order to have an idea how the missing information of the impedance phase angle affects the simulation result, surface impedance boundary condition is prescribed at the ground of the finite element model using varying impedance phase angle.

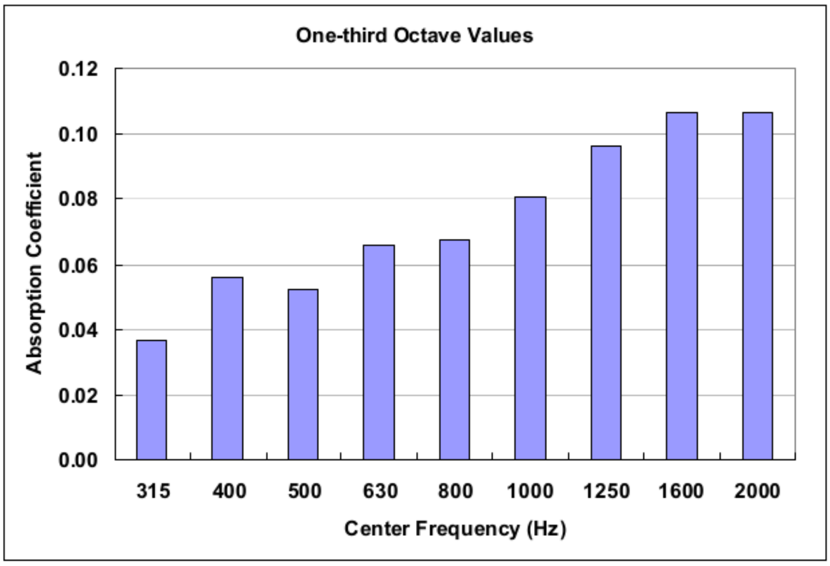

Figure 4.11: Absorption coefficient in one-third octave bands taken from [6].

Due to a missing ground absorption measurement, the absorption spectrum from the pavement absorption measurement carried out by Seybert et al. [6] is used, which is shown in Fig. 4.11. The values of the absorption coefficients are estimated from the graph and are listed in Tab. 4.6 since these were not provided in the paper. For frequencies lower than 315 Hz, the absorption coefficient is set to 0.02. The complex normalized surface impedance can then be calculated by solving the system of equations consists of Eq. (4.18) and Eq. (4.19). Thereby, the impedance phase angle φ is assumed to be $0°$ (only real part), $\pm30°$, $\pm45°$, and $\pm60°$, respectively. The resulting normalized surface impedance spectra for different impedance phase angles are shown in Fig. 4.12.

Table 4.6: Estimated absorption coefficient from Fig. 4.11, for frequencies lower than 315 Hz the values are set to 0.02.

Frequency (Hz)	α	Frequency (Hz)	α
100	0.02	500	0.05
125	0.02	630	0.065
160	0.02	800	0.065
200	0.02	1000	0.08
250	0.02	1250	0.095
315	0.035	1600	0.105
400	0.055	2000	0.105

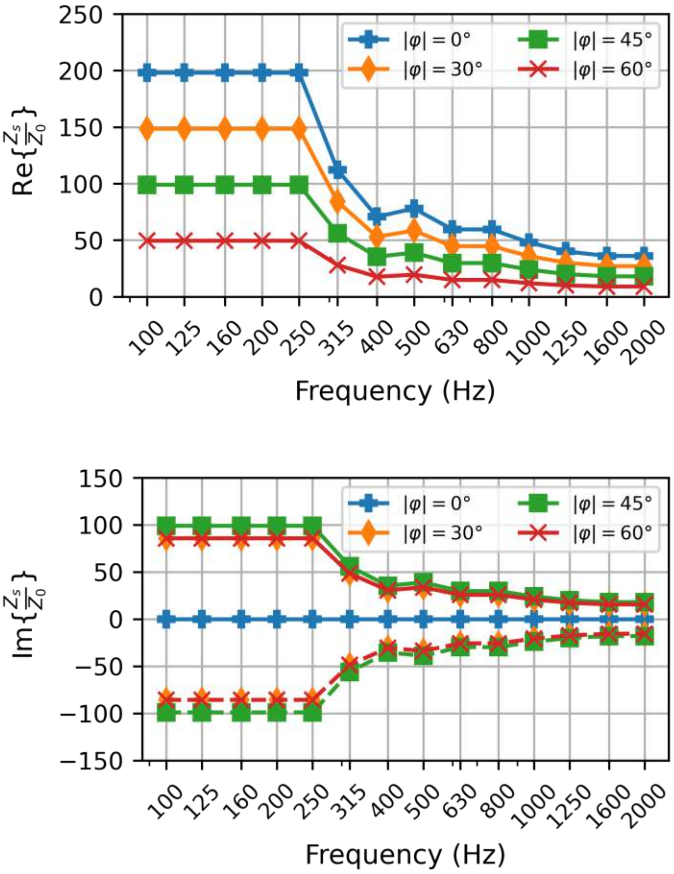

Figure 4.12: Real and imaginary part of the surface impedance normalized by $Z_0 = \rho_0 c_0$ calculated by solving Eq. (4.18) and Eq. (4.19).

4.3.3 Variation of frequency steps per 1/3-octave band

In this thesis, the simulation and the measurement results will be compared in one-third octave bands. In the initial simulation setup, each one-third octave band is computed using nine intermediate frequency steps corresponding to the 1/24-octave center frequencies to ensure a sufficient frequency band resolution. However, the computation time of single one-third octave band grows almost linearly with the number of intermediate frequency steps. As already shown in Section 4.1, the computation time of the highest frequency band 2000 Hz using nine intermediate frequencies almost takes up half of the total simulation run time. Therefore, it is of great interest to find a proper number of intermediate frequency steps per one-third octave band, which can lower the computational effort of the simulation while providing a similar numerical accuracy.

For the parametric study, each one-third octave band is computed using one, three, five, and nine intermediate frequency steps, respectively. Obviously, there are several possibilities for choosing the frequencies used within the octave band. However, this study concentrates on the influence of the number of frequencies used on the simulation results but not the different selection of the frequencies. Therefore, a rule for choosing the frequencies used within the one-third octave band will be defined for each number of steps. For the single frequency step, the center frequency of the corresponding one-third octave band is used. Next, for the model using three intermediate steps, the lower and the upper frequency limits of the one-third octave band are additionally used, corresponding to the 1/6-octave center frequencies. Finally, the frequencies used for five steps and nine steps are equivalent to the 1/12-octave center frequencies and the 1/24-octave center frequencies within the one-third octave frequency band, respectively. An example of the frequency selection for 1000 Hz one-third octave band is shown in Tab. 4.7. The same selection criteria apply to other one-third octave bands.

Table 4.7: Choice of frequencies used for different number of intermediate steps, example one-third octave band 1000 Hz.

Number of steps	Frequencies used (Hz)	Note
1	1000	1/3-octave center frequency
3	891, 1000, 1122	1/6-octave center frequencies
5	891, 944, 1000, 1059, 1122	1/12-octave center frequencies
9	891, 917, 944, 972, 1000, 1029, 1059, 1091, 1122	1/24-octave center frequencies

Chapter 5

Results and Discussions

In the following, the results obtained from the finite element simulation using different setups are discussed and compared to the outer pressure field measurement.

5.1 Comparison of simulation and measurement results

In Fig. 5.1, the A-weighted sound pressure levels at measurement position a (10 cm away from vehicle) along the carbody height for various one-third octave bands are shown. The simulation result is compared with the measurement value at each microphone position. One can see that for 125 Hz and 400 Hz, the simulation fits the measured curves very well. A greater difference between the simulation and the measurement occurs for 1250 Hz and 2000 Hz, but the measured shape is still well approximated for both frequency bands. Other bands show similar results, and the model captures the measured sound pressure level trends well.

The overall sound pressure level is a simple and direct parameter to quantify the sound level. For this comparison, the A-weighted sound pressure levels of each one-third octave band from 100 Hz to 2000 Hz are added up in decibels, yielding the *overall SPL*. Figure 5.2 shows the overall A-weighted sound pressure level at three different measurement positions and the deviation between the simulated and measured results. As can be seen from the results, the predictions of overall sound pressure levels at the three distances from the car body agree well with the measurement. For all three measurement positions, the maximum deviation between the simulation and measurement results occurs at 0.5 m, which is at the height of the bogie. At these locations, the simulation results are 1.5 dB to 3 dB higher than the measured values. In general, the approximation improves with increasing height. In the area above 2 m, the difference between the simulation and the measurement in terms of overall sound pressure is within 1 dB.

Figure 5.3 shows the spectra of the A-weighted sound pressure level in one-third octave bands. The SPL spectra are evaluated at the measurement position a (10 cm away from the vehicle) at various heights. As can be seen from the results, the simulation fits the measured spectra well, the measured trend is well captured. Again, a larger deviation between the simulated and measured results occurs at 0.5 m above ground and the approximation is getting better with increasing height.

In order to have an idea of the model accuracy of each 1/3-octave band, the mean relative error between the simulation result and the measurement for each 1/3-octave band over all 27 microphone positions will be computed. To compute the mean relative error, the sound pressure level is first converted back to linear scaling by

$$p(\mathrm{Pa}) = p_0 \cdot 10^{\frac{\mathrm{SPL}}{20}} = 2 \cdot 10^{-5}\,\mathrm{Pa} \cdot 10^{\frac{\mathrm{SPL}}{20}}. \tag{5.1}$$

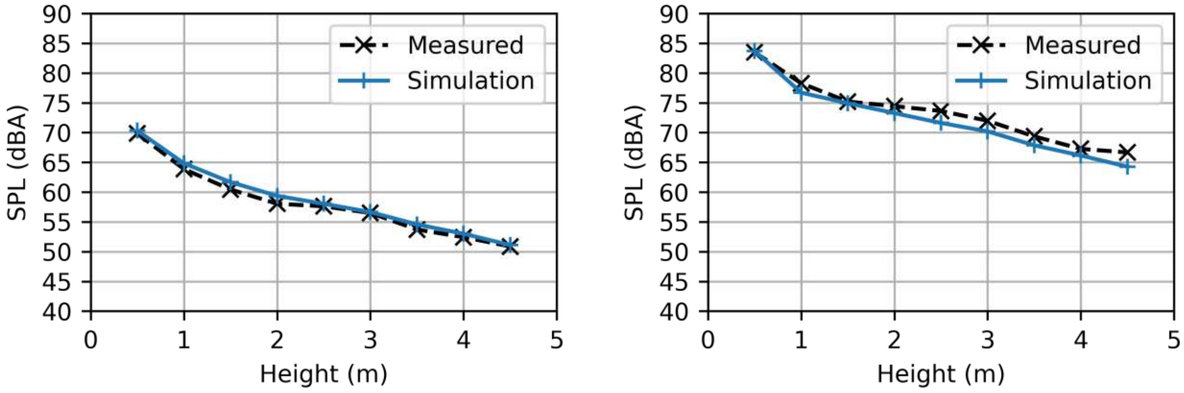

(a) 125 Hz

(b) 400 Hz

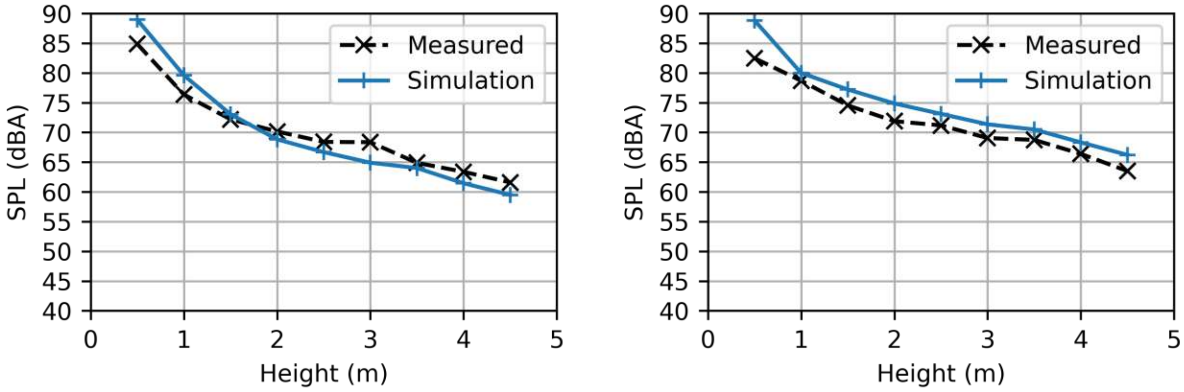

(c) 1250 Hz

(d) 2000 Hz

Figure 5.1: Comparison between simulation (full line) and measurement (dashed line) over the height at measurement position a (10 cm away from the carbody wall) for various one-third octave bands. A-weighted SPL in dBA ref 20 µPa.

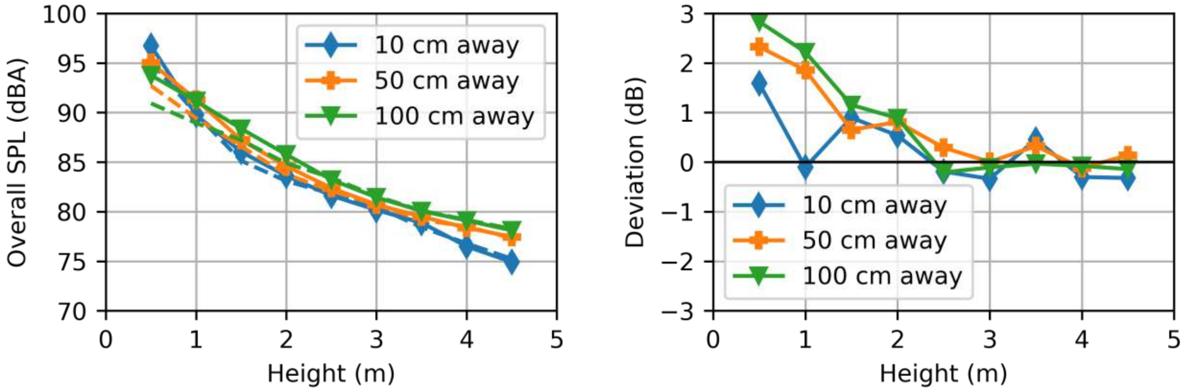

Figure 5.2: Comparison between simulation (full lines) and measurement (dashed lines) over the height at various measurement positions. Left: Overall SPL in dBA ref 20 µPa; Right: Deviation between simulation and measurement results.

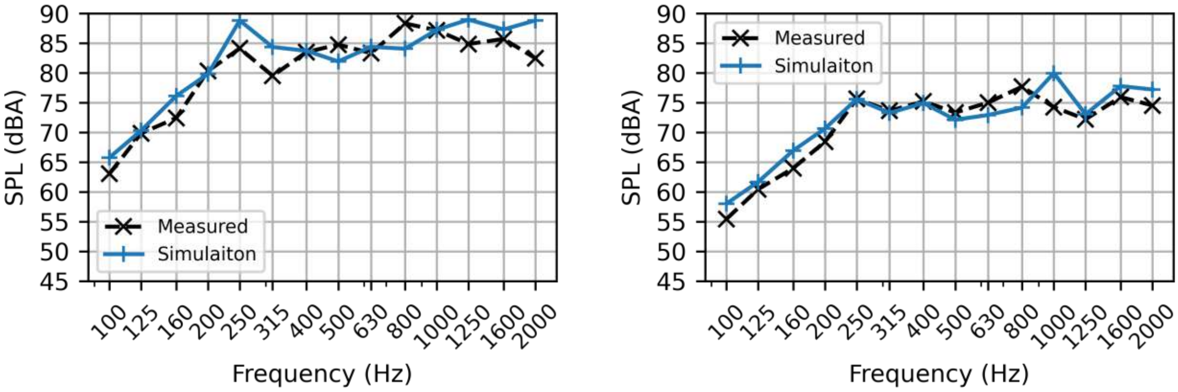

(a) 0.5 m

(b) 1.5 m

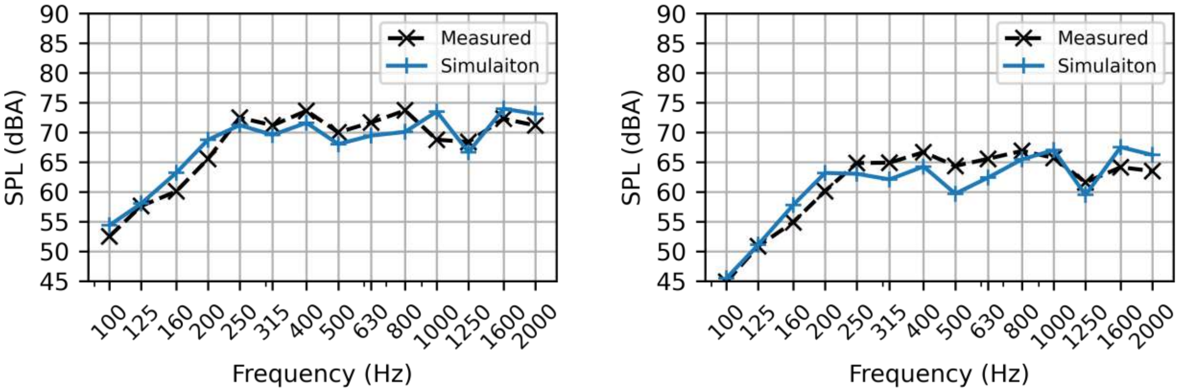

(c) 2.5 m

(d) 4.5 m

Figure 5.3: Comparison of the A-weighted SPL spectra between simulation (solid line) and measurement (dashed line) evaluated at measurement position a (10 cm away from the carbody wall) at various heights above ground.

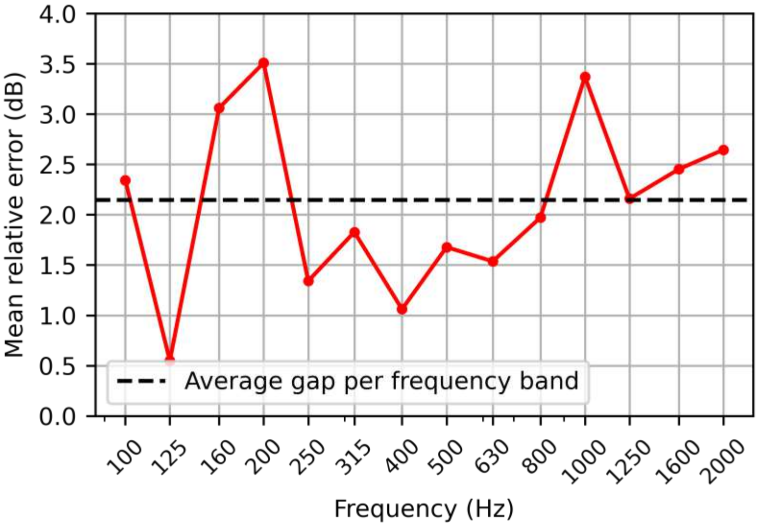

Figure 5.4: Mean relative error between simulation result and measurement for each 1/3-octave band over all 27 microphone positions.

Table 5.1: Mean relative error of 1/3-octave frequency spectrum over all microphone positions.

Frequency (Hz)	MRE (dB)	Frequency (Hz)	MRE (dB)
100	2.34	500	1.67
125	0.55	630	1.53
160	3.06	800	1.97
200	3.51	1000	3.36
250	1.34	1250	2.15
315	1.82	1600	2.45
400	1.06	2000	2.65

The mean relative error (MRE) is then defined as

$$\mathrm{MRE}(p_{\mathrm{measured}}, p_{\mathrm{simulation}}) = \frac{1}{N}\sum_{i=0}^{N-1}\frac{|p_{\mathrm{simulation},i} - p_{\mathrm{measured},i}|}{|p_{\mathrm{measured},i}|}\,. \tag{5.2}$$

The mean relative error can also be converted to decibels using the relation

$$\mathrm{MRE(dB)} = 20 \cdot \log_{10}(1 + \mathrm{MRE})\,. \tag{5.3}$$

The mean relative error in terms of the sound pressure levels over all 27 microphone positions at each frequency band between the predictions and the measurements are shown in Fig. 5.4 and in Tab. 5.1. As can be seen from the results, the best approximation occurs for the 125 Hz band which has the smallest mean relative error among all 1/3 octave bands. Three frequency bands (160 Hz, 200 Hz and 1000 Hz) have an error over 3 dB, and the maximum error is limited by 3.5 dB. Good approximation has also been shown for the frequency bands from 250 Hz to 800 Hz, for which the mean relative errors are within 2 dB. The average gap per frequency band is obtained by averaging the mean relative error spectrum over all 14 one-third octave bands. Following the same idea, the mean relative error in terms of overall sound pressure levels will also be used as a metric for model accuracy.

The average gap per frequency band and the mean relative error of overall sound pressure levels over all microphone positions are shown in Tab. 5.2. The average difference per frequency band is 2.14 dB

Table 5.2: Average gap per frequency band and mean relative error of overall SPL of the initial model.

Average gap per frequency band (dB)	Mean relative error of overall SPL (dB)
2.14	0.73

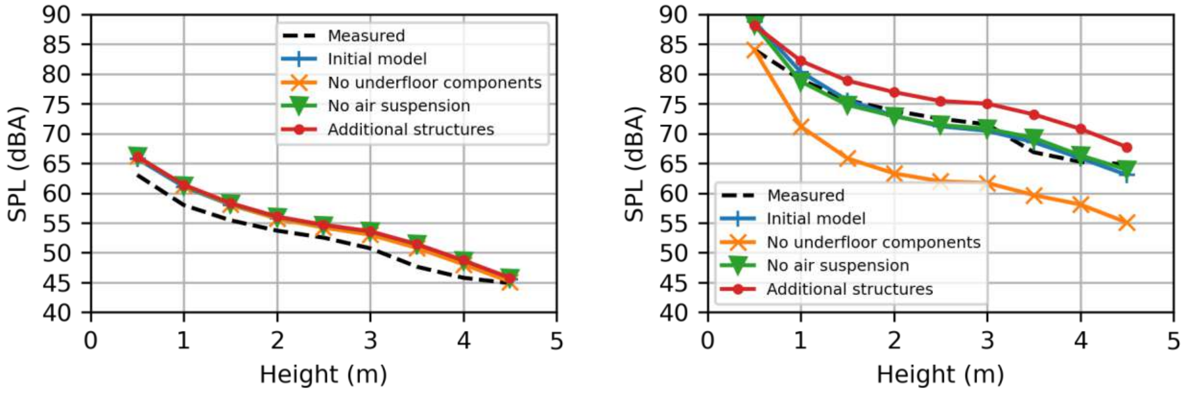

(a) 100 Hz

(b) 250 Hz

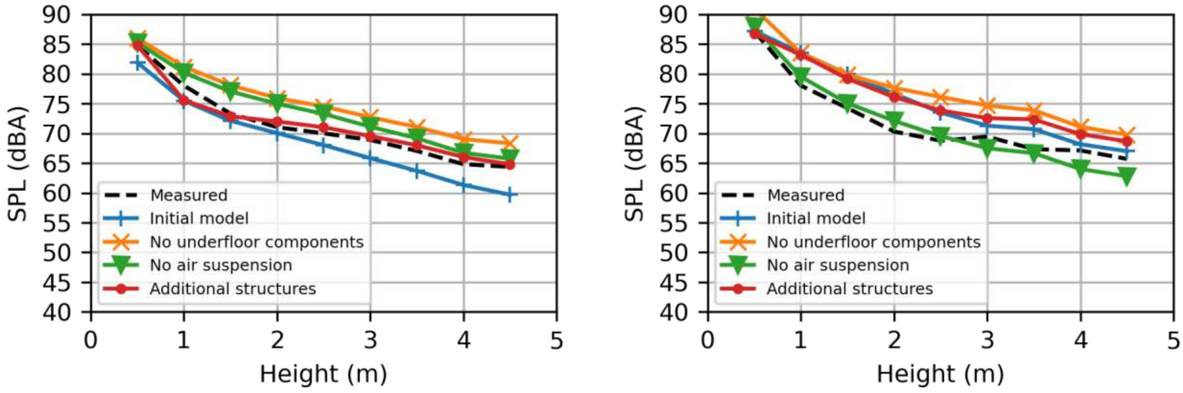

(c) 500 Hz

(d) 1000 Hz

Figure 5.5: Sound pressure level over the height at measurement position a, comparison between different geometrical models (solid lines) and the measurement (dashed lines). SPL in dBA ref 20 µPa.

and the mean relative error of the overall sound pressure level is 0.73 dB. From these results, it can be concluded that the finite element model is able to predict the sound transmission from the train underfloor with adequate accuracy.

5.2 Effect of geometric variation

In this section, the results obtained by the variation analysis of underfloor geometry are shown. The geometrical models are illustrated and explained in Section 4.3.1.

Figure 5.5 shows the A-weighted sound pressure level at measurement position a (10 cm away from vehicle) for different geometry variations in example one-third octave bands. As can be seen from the results, there is almost no difference between the different models at the lowest frequency band (100 Hz). This may be because the wavelength (about 3.43 m for 100 Hz) is much larger than the characteristic physical dimensions of the geometry. At this frequency, all four models overestimate the sound pressure

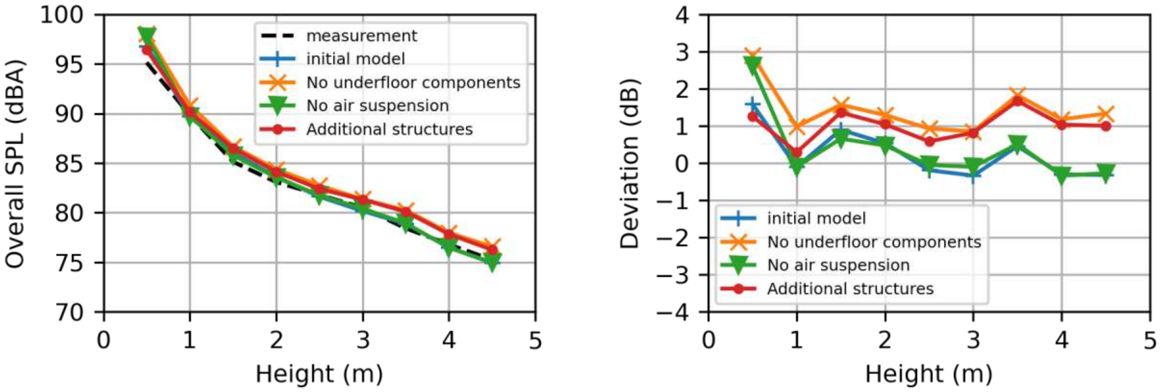

(a) 10 cm away from carbody.

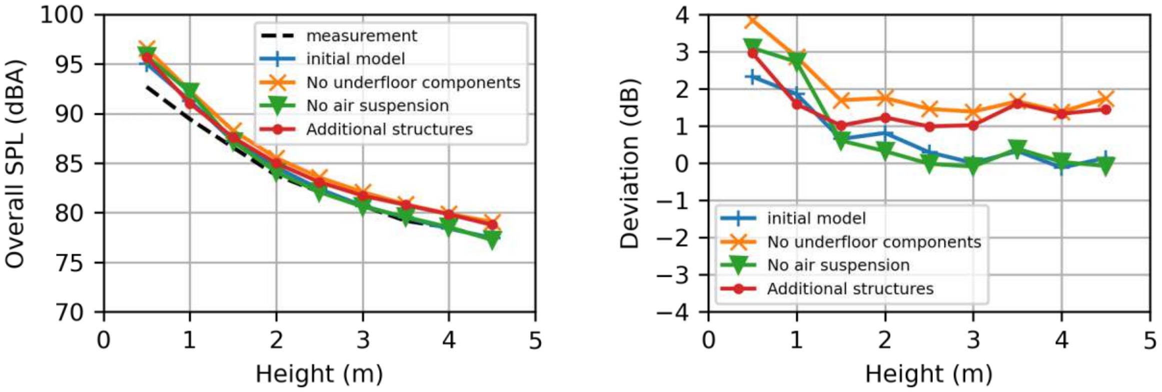

(b) 50 cm away from carbody

Figure 5.6: Comparison between simulation (solid lines) and measurement (dashed lines) over the height at various measurement positions for different geometrical models. Left: Overall SPL in dBA ref 20 µPa. Right: Deviation between simulation and measurement results.

level by about 3 dB but are still able to capture the measured curve shape well. A large deviation between the models is found at 250 Hz, where the model without underfloor components underestimates the measurement result and the model with additional structures tends to overestimate them. The initial model and the model without air suspension show very good agreement with the measurement data. For 500 Hz and 1000 Hz, the model with additional structures and the model without air suspension agree well with the measurement data. In general, all models show similar shapes as the measurement curves, the differences in terms of sound pressure level between the four models are within 10 dB. Very similar results are also observed for other frequency bands.

Figure 5.6 shows the distribution of A-weighted overall sound pressure levels at different distances from the carbody for different geometrical models. As can be seen from the figures, all four models show similar results in the lower area (up to 2 m height), the deviation between the models starts to grow with increasing height. Comparing the initial model and the model without air suspension, the model without air suspension shows a greater overestimation of the overall SPL than the initial model at the height of the bogie (0.5 m). Up from 1.5 m height, both models show very good agreement with the measurement results and there is almost no difference between both models. One can also see that without including any underfloor components in the model, the overall SPL is overestimated at each measurement location due to a lack of shielding of the acoustic wave by the underfloor components. The difference between the

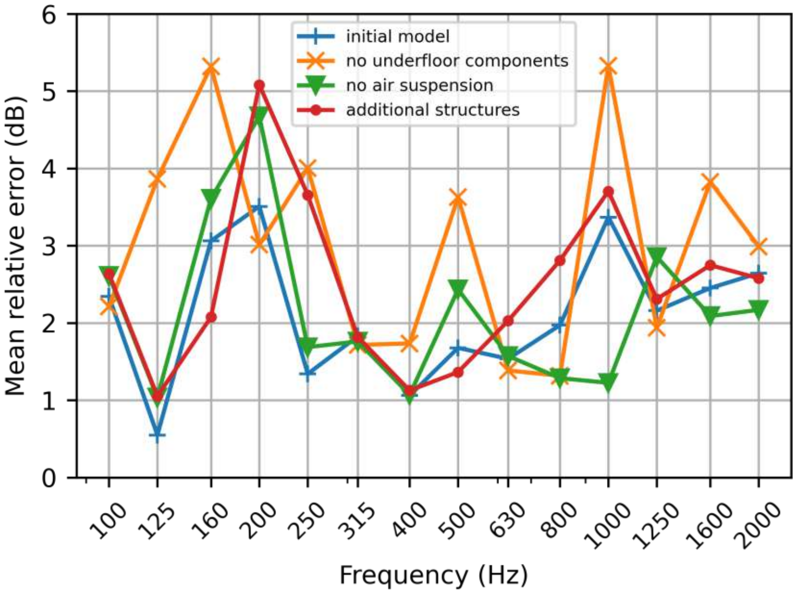

Figure 5.7: Mean relative error of 1/3-octave frequency for different geometry variations.

Table 5.3: Average gap per frequency band and mean relative error in overall SPL for different geometry variations.

Geometry name	Average gap per frequency band (dB)	MRE overall SPL (dB)
No underfloor components	3.12	1.78
No air suspension	2.21	0.85
Initial model	2.34	0.73
With additional structures	2.57	1.30

initial model and the model without underfloor components is about 1 dB to 1.5 dB, depending on the measurement locations. The model with additional underfloor structures shows a similar result as the initial model at 0.5 m height, but in the higher region (up from 1.5 m), the result converges to that of the model without underfloor components.

Figure 5.7 shows the mean relative error spectra for the four geometrical models over all 27 microphone locations. The spectrum of the initial model has also been shown in Fig. 5.4. As can be seen from the figure, all three geometry variations show greater maximum error than the initial model. For a large part of the frequency bands, the model without underfloor components has the greatest deviation among the models. At frequency band 100 Hz, 315 Hz, 400 Hz, 630 Hz and 2000 Hz, the difference in terms of the mean relative error among the models is small and limited by 1 dB. The initial model and the model without air suspension share similar results, but at frequency band 800 Hz, 1000 Hz, 1600 Hz and 2000 Hz, the latter model shows better approximation than the former.

In order to quantify the difference between the geometry variations, the average gap per frequency band and the mean relative error in terms of overall SPL are computed and shown in Tab. 5.3. The table is ordered by the complexity of the modeled geometry. As can be seen from results, the simplest model, namely the model without any underfloor components, shows the greatest average gap per frequency band as well as the largest mean relative error in terms of the overall sound pressure level. Both errors are reduced by almost 1 dB by including the most essential underfloor components (bogie and wheel) into the model. Taking the air suspension into account leads to a better approximation for the overall SPL, but a slightly increased average gap per frequency band, which may be due to the assumption of a sound hard boundary at the air suspension interface. Surprisingly, the model with additional structures shows a greater deviation in both metrics compared to the initial model. It was expected that including more underfloor details will also lead to a better approximation of the measurement. It can be concluded from the results shown in this section that the number of modeled underfloor components affect the prediction accuracy of the finite element model. To achieve better approximation of the measurement data, the bogie and the wheel at a minimum should be taken into the geometrical model. Without modeling the underfloor components, the predicted overall SPL is about 1 dB higher compared to the prediction using model with underfloor components.

5.3 Effect of ground absorption

In this section, the simulation results obtained by the variation analysis of the surface impedance are shown. Note that all variation models have the same normal incident absorption coefficient and only differ in their impedance phase angle. Since the absorption data used for the simulation is fictive, the results are not compared to the validation measurement but to the initial model with fully reflective ground.

Figure 5.8 shows the A-weighted sound pressure level at measurement position a (10 cm away from vehicle) along the carbody height for models with different impedance phase angles in example one third octave bands. The simulation results are compared to the result obtained by the model without ground absorption (initial model) and the difference is also shown in the figures. As can be seen from the results, for 100 Hz, there is almost no noticeable difference between the absorption models and the initial model due to the small absorption coefficient (2 %) in the low frequency range from 100 Hz to 250 Hz. For frequencies with higher absorption coefficients, a decrease in sound pressure level due to absorption becomes more visible. One can see that the degree of absorption within a frequency band strongly depends on the phase angle of the complex surface impedance. In general, the greater the impedance angle the stronger the absorption. An exception exists for the model with zero phase angle, which contains only a real valued part, its curve lies between those of positive and negative 45-degree angles. Also, it can be seen that the attenuation also depends on the sign of the impedance phase angle, the negative angle (dashed line) leads to a slightly stronger attenuation than its complex conjugate (solid line), and the difference between the complex conjugate pair grows with the absolute phase angle. For phase angles with the same sign, they share the same curve shape, and only differ in their absolute values.

Very similar results are also observed in the overall sound pressure level distribution, which is shown in Fig. 5.9. Again, the impedance phase angle dependency of the absorption can be seen from the results, i.e., the greater the phase angle, the greater the deviation to the full reflective model and hence, the higher the attenuation. The greatest difference in terms of overall sound pressure level among the investigated phase angles is about 1 dB. Furthermore, a complex conjugate pair with the same absolute impedance phase angle with a negative phase angle (dashed line) shows higher attenuation than the positive one (solid line). Furthermore, the deviation among the conjugate pair grows with the absolute phase angle. In the case of zero phase angle whose surface impedance contains only real part, its result lies between those of the 45-degree complex conjugate pair.

Figure 5.10 shows the mean relative deviation spectra in terms of sound pressure level for different impedance phase angles compared to the initial model with fully reflective ground. As can be seen from the results, in low frequency region between 100 Hz and 315 Hz, where the absorption coefficient is small (2 % to 3 %), the difference in results between the different phase angles is also small. With growing absorption coefficient, the deviation between the phase angles gets larger. The largest difference occurs in the high frequency region, in this case between 1000 Hz and 2000 Hz, where the deviation is about

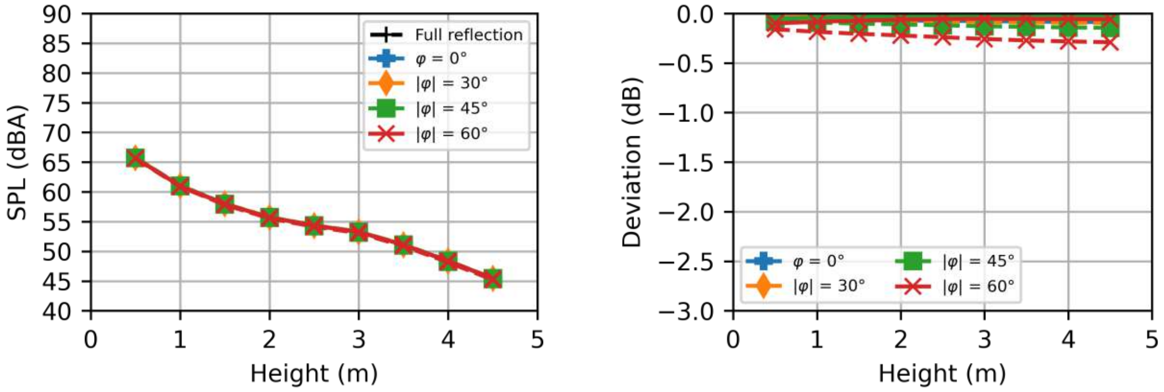

(a) 100 Hz

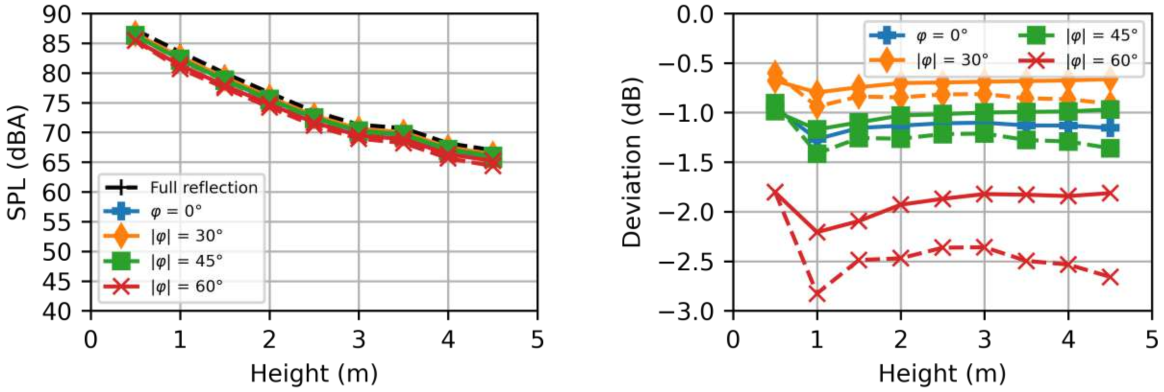

(b) 1000 Hz

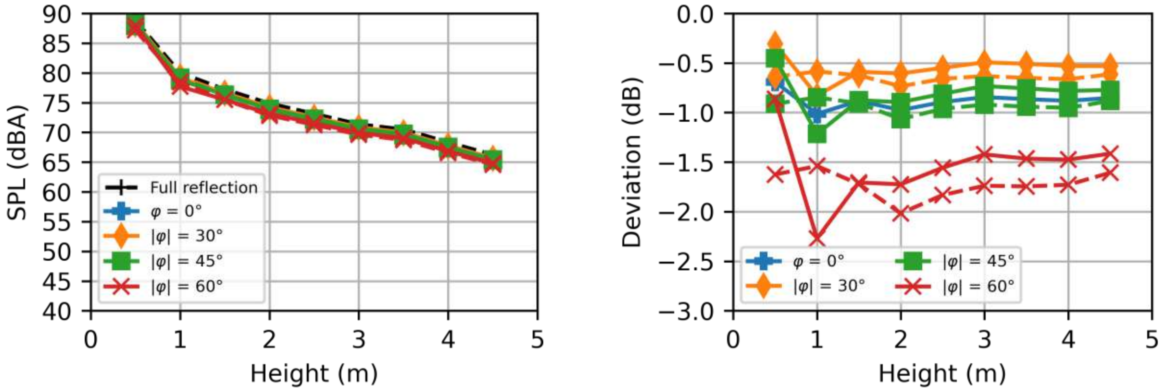

(c) 2000 Hz

Figure 5.8: Sound distribution over the height at measurement position a, comparison between the model with full reflective ground (black dashed lines) and the models with different impedance phase angles (colored lines). Colored solid curves: positive phase angle; Colored dashed curves: negative phase angle.

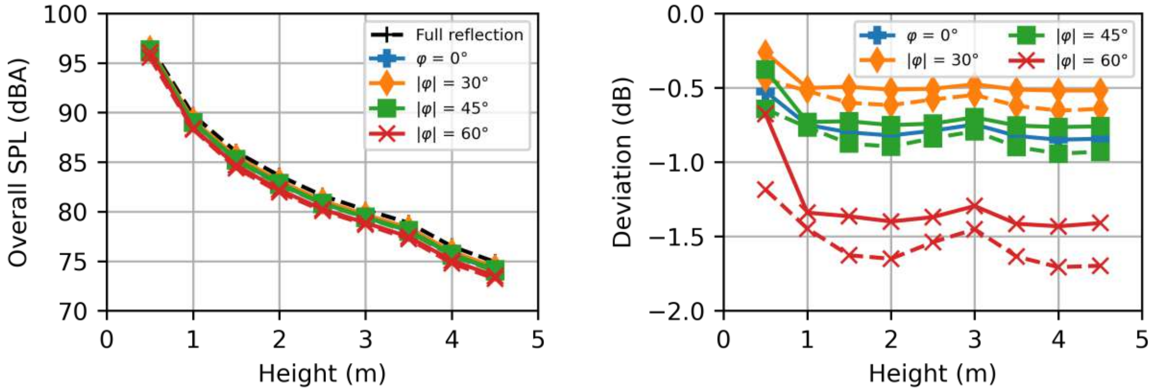

(a) 10 cm away from the car body

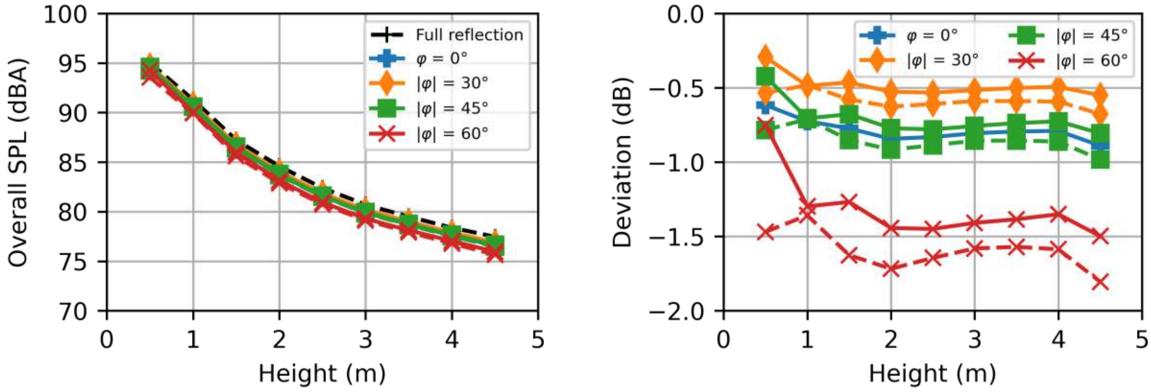

(b) 50 cm away from the carbody

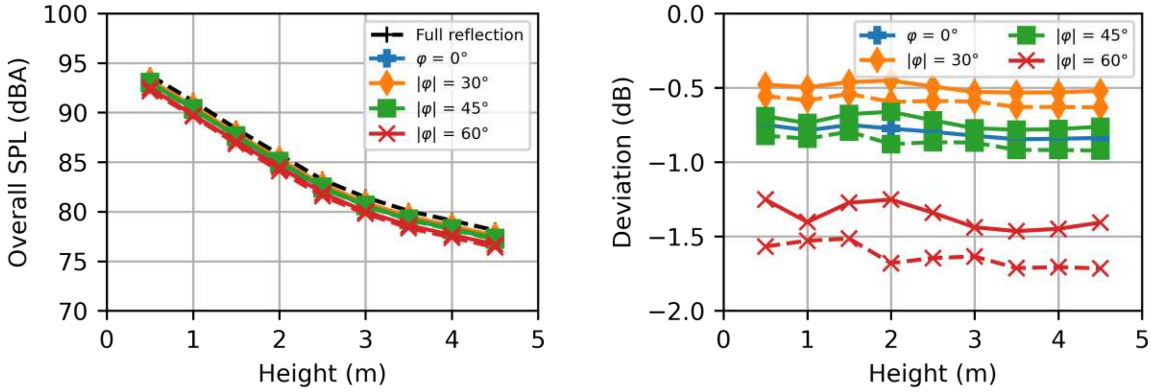

(c) 100 cm away from the carbody

Figure 5.9: Comparison of overall A-weighted sound pressure level between difference impedance phase angles at various measurement positions. Solid lines: positive phase angle; dashed lines: negative phase angle.

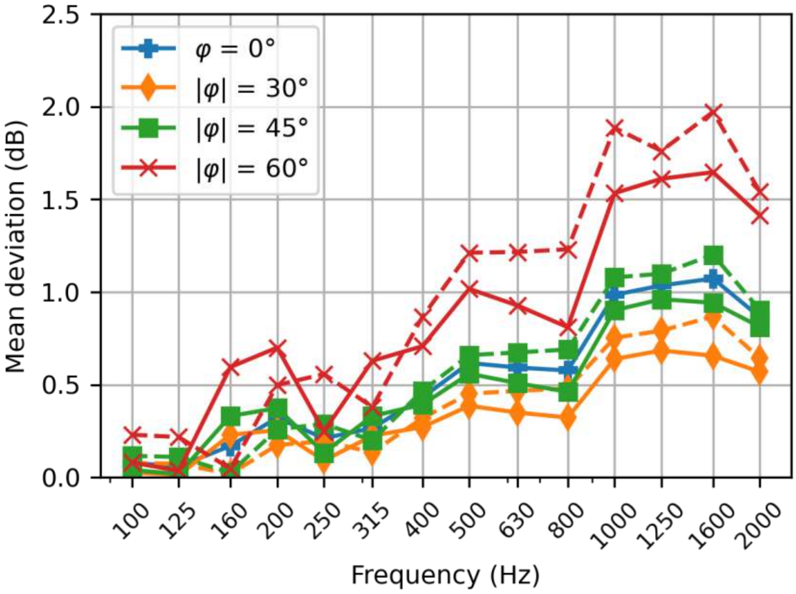

Figure 5.10: Mean relative deviation in terms of sound pressure level compared to full reflective model in 1/3-octave bands. Solid lines: positive phase angle; dashed lines: negative phase angle.

Table 5.4: Mean deviation in overall SPL for different impedance phase angles.

$\arg(\tilde{R}_s + j\tilde{X}_s)$ (°)	Average deviation in overall SPL (dB)
0	0.72
30/-30	0.46/0.55
45/-45	0.66/0.78
60/-60	1.15/1.34

1.5 dB.

The average deviation in terms of overall sound pressure level compared to the full reflective model can be found in Tab. 5.4. A larger deviation to full reflective model means a larger absorption of the sound pressure. One can see that the difference between the smallest and the largest absorption degree is about 1 dB. Additionally, the absorptance of 0-degree angle is the median of the result set.

From the results shown in this section it can be concluded that for a given normal incident absorption coefficient spectrum, the actual attenuation of the acoustic wave depends on the phase angle of the complex surface impedance. For a given absorption coefficient with a value of 0.1, the actual attenuation of the pressure obtained varies from about 0.5 dB to 2 dB depending on the investigated impedance phase angles. In cases where only data for the absorption coefficient is available, it can be assumed that the surface impedance contains only a real part. The same approach is also used by Li et al. [8] in their finite element analysis for rail acoustics to handle the unknown impedance phase angle. In order to obtain a more accurate simulation result, not only should the absorption spectrum of the material be provided, but also the full impedance characteristic of the ground surface. This information can be obtained by, e.g., an in-situ measurement of surface impedance using impedance tube method as described in [37, 38].

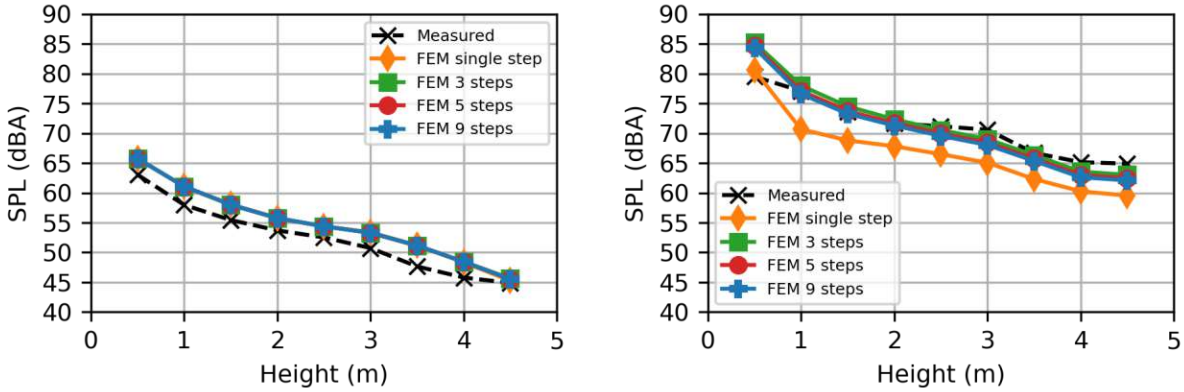

(a) 100 Hz

(b) 315 Hz

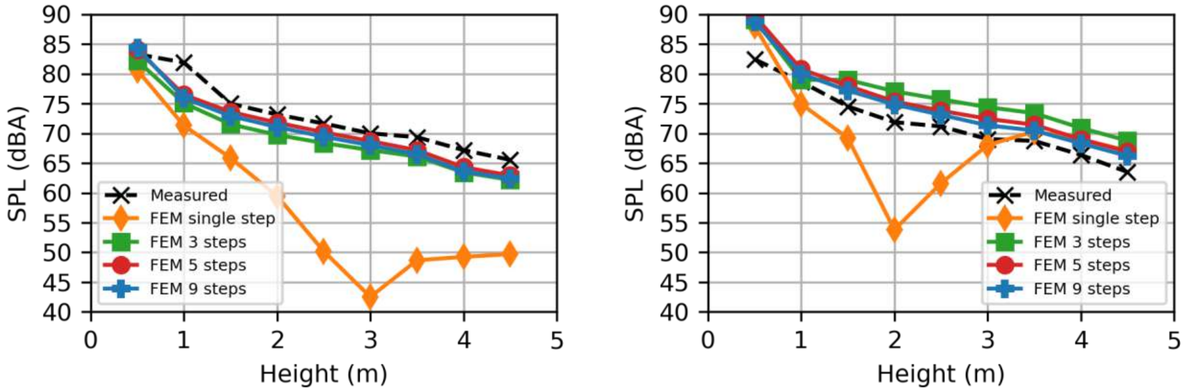

(c) 630 Hz

(d) 2000 Hz

Figure 5.11: A-weighted sound pressure level over the height at measurement position a, comparison between measurement (dash lines) and simulation (solid lines) using different intermediate steps per one-third octave band.

5.4 Effect of varying frequency steps per 1/3-octave band

In this section, the simulation results obtained by variation analysis using different intermediate frequency steps in single 1/3-octave band are shown.

Figure 5.11 shows the sound distribution at measurement position a (10 cm away from vehicle) along the height direction for different frequency resolutions of one-third octave bands. As can be seen from the results, there is almost no noticeable difference in results for 100 Hz between the different frequency steps due to its narrow bandwidth of about 23 Hz, and a high ratio of wavelength to geometry feature length could also be a reason. With increasing one-third octave band frequency and hence an increasing bandwidth, using one single intermediate frequency step to resolve the one-third octave band is not enough. At 315 Hz, the predicted sound pressure level using only a single step is about 5 dB lower than the results obtained with more frequency steps. In the 630 Hz and 2000 Hz bands, when using only the center frequency to represent the one-third octave band, a destructive interference effect in the sound distribution can be observed. The sink in the sound pressure curve is smoothed out once more intermediate frequency steps are used to compute the one-third octave band result. Except for the single step, results obtained by using 3, 5 and 9 intermediate steps are in the same range and agree well with the measurement.

Figure 5.12 shows the pressure field of three frequencies within the 2000 Hz one-third octave band.

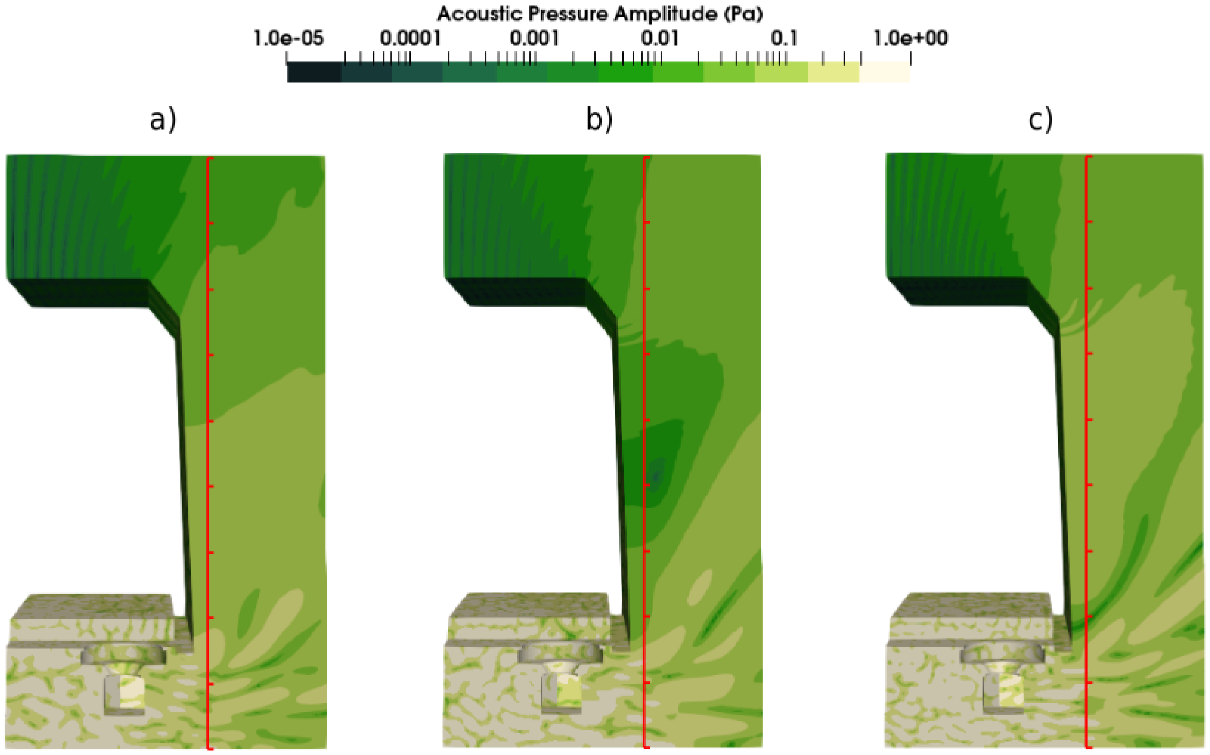

Figure 5.12: Acoustic pressure amplitude field for three frequencies in 2000 Hz one-third octave band. a) 1781 Hz; b) 2000 Hz; c) 2245 Hz. The vertical red line indicates the evaluation position (10 cm from the car body) over the domain height.

Table 5.5: Mean relative error in overall SPL and total computation time using different intermediate frequency steps per one third octave band.

Number of intermediate steps	MRE in overall SPL (dB)	Total computation time (h)
1	1.10	4.5
3	0.82	10
5	0.76	15
9	0.73	27

The frequencies are corresponding to the lower band limit, the center frequency and the upper band limit of the one-third octave band, respectively. The sink in the sound pressure level curve using only single step as shown in Fig. 5.11d is due to the destructive interference of the acoustic wave, which can be seen in the pressure field corresponding to 2000 Hz. The dark green at the middle of the carbody wall indicates a sink in the acoustic pressure. If more intermediate frequency steps are used, the sink in the sound pressure level curve will get averaged out since no destructive interference occurs at the same location in the pressure field of other frequencies.

Figure 5.13 shows the overall A-weighted sound pressure level distribution obtained by using different intermediate frequency steps compared to the measurement. As can be seen from the figures, at most of the microphone locations the simulation using nine frequency steps per one-third octave band shows the closest fit to the measurement while the results obtained by using three or five intermediate steps are also in the same range, but with a slightly greater deviation. When using only one single frequency step, a noticeable difference to the measured SPL curve at 2 m to 4 m height can be observed. This is also the range of the height in which for several one-third octave band center frequencies the sinks in sound pressure level curves are located, as previously shown in Fig. 5.1.

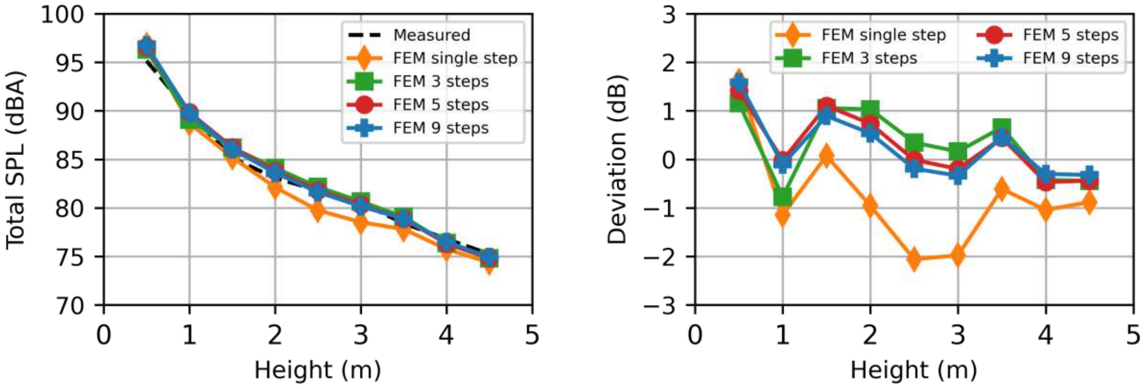

(a) 10 cm away from the carbody

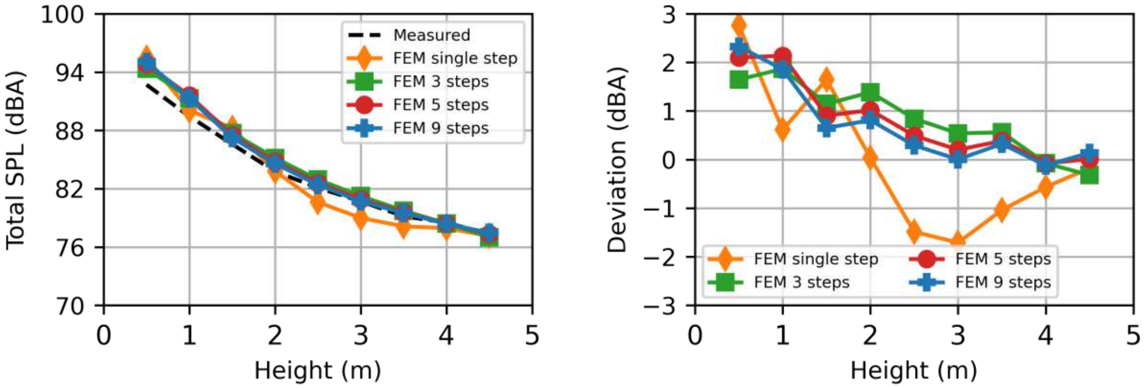

(b) 10 cm from the carbody

Figure 5.13: Comparison between simulation (full lines) using different intermediate frequency steps per one-third octave band and measurement (dashed lines) over the height at various measurement positions. Left: Overall SPL in dBA ref 20 µPa; Right: Deviation between simulation and measurement results.

Tab. 5.5 shows the mean relative error in terms of the overall A-weight sound pressure level to the measurement obtained by using different intermediate frequency steps per one-third octave band. Further, the total computation time for all 14 one-third octave bands covering 100 Hz to 2000 Hz is also shown in the same table. As expected, the more intermediate steps per one-third octave band are used, the better the approximation to the measured results. On the other hand, it can be seen that the convergence rate of the mean relative error is getting slower with increasing intermediate steps, which means upon a certain degree of frequency resolution, a better approximation cannot be achieved by simply using more intermediate frequency steps per one-third octave band. Another important aspect of choosing the proper number of intermediate frequency steps is the total computation time of the simulation, which increases linearly with the number of frequency steps. For our finite element model, choosing five intermediate steps per one-third octave band would be a good compromise between accuracy and computational effort, since it has a similar mean relative error in terms of overall sound pressure level as the initial setup with nine intermediate steps but saves up almost 50 percent of the computation time.

From the results shown in this section, it can be concluded that the number of intermediate frequency steps used per one-third octave band affects the prediction accuracy of the finite element model. In the low frequency range, using one single frequency step to resolve the one-third octave band is sufficient while with increasing frequency, more intermediate steps are needed to obtain a good approximation to the measurement result. For the investigated finite element model, there is no noticeable difference in terms of overall sound pressure level between the simulation results obtained by using three, five, and nine intermediate steps, respectively. All three setups show good agreement with the measurement data and differ in their total computation time. For the investigated frequency range from 100 Hz to 2000 Hz, using five intermediate steps to resolve the one-third octave band is a good compromise between simulation accuracy and computational effort.

Chapter 6

Summary and Future Work

This chapter summarizes the conducted work for this thesis and presents topics that remain as future work due to the limited scope of the thesis.

Summary

This thesis aimed to develop a computational model that is capable to predict the noise propagation from the railway vehicle underfloor area into the external environment around the vehicle car body using finite element method and consequently to validate the model by comparing simulation results with the measurement data. In this thesis, the modeling approach was applied to the metro train model X-Wagen from the manufacturer Siemens. Due to the large dimension of the vehicle, the area of interest for the simulation was confined to a segment of the metro car, which was chosen to be the front part of the metro head car where the non-driven bogie is located. The symmetry of the car body cross-section was exploited and the considered car segment was represented by a one-fourth model to reduce computational effort.

The actual geometry of the finite element model was then obtained by cutting the car segment out of an air volume. A proper simulation domain size was found through a parameter study on the domain width. To simulate the open exterior domain, the perfectly matched layer (PML) technique was applied to the model using three quadratic elements in the layer thickness direction to ensure a stable performance of the PML. The acoustic domain of the model was separated into a sub-region containing complex surface geometries and a main propagation region. The former sub-region was meshed with tetrahedral elements and the latter with hexahedral elements, respectively. Both sub-regions were coupled by non-conforming interfaces. To reduce discretization error, second-order elements were used globally for the mesh. The frequency range of interest for the simulation was 100 Hz to 2000 Hz resolved in one-third octave bands. To reduce the computational cost, four different grids using a frequency-dependent discretization size were prepared for the harmonic simulation. By all measures, the computational cost of the finite element model was able to be kept in an adequate range with a total computation time of about 26 hours using 32 physical CPU cores if the simulations were executed in sequential order. The actual solve time of the model was shortened to about 14 hours with carefully chosen allocation of the simulation jobs. The memory requirement ranged from 20 GB to 260 GB depending on the used grid size. It could be shown that for a given amount of available memory, the upper analyzable frequency band is related inversely to the simulation domain size.

As part of this thesis, the acoustic power measurement of the sound source used and the outer pressure field measurement around the carbody were carried out. The former measurement provided necessary information for the input excitation for the simulation while the latter served as reference solutions for the finite element model. The simulations were done using the open-source FEM software openCFS. The obtained results showed a good agreement with the validation measurement. Thereby, the average deviation per frequency band was 2.4 dB. In terms of the overall sound pressure level, the mean relative error over 27 evaluation points around the car body was 0.7 dB. It can be concluded from the obtained results that the developed finite element model is able to predict the outer field pressure distribution due to the vehicle underfloor noise with acceptable accuracy.

Besides the validation of the developed finite element model, several parametric studies have been carried out within this thesis that aimed to investigate the sensitivity of the simulation results with respect to the variation of several model parameters. During the design process of the finite element model, a parameter study aimed at finding the proper size of the exterior acoustic domain was performed. It has been shown that for our problem of interest, using a domain width of 1 m could already provide good numerical accuracy without extensively increasing the computational cost. The study also showed that if the area of interest moved toward the roof of the vehicle, the domain width has to be extended in order to ensure a sufficient width-to-height ratio of the propagation region, which could be a useful hint for the future model design. The results obtained from the variation of the underfloor geometry pointed out that the number and type of considered underfloor components in the finite element model could affect the prediction results. Without taking the bogie into account, the simulated overall sound pressure level was overestimated at each evaluation position by about 1 dB compared to the initial finite element model, which was still in an acceptable range. To increase the prediction accuracy, at a minimum the essential underfloor components, i.e., the bogie frame and the wheel should be included to ensure a sufficient shielding of the acoustic wave in the underfloor area. The inclusion of a fictitious ground absorption into the model showed that the actual attenuation of the acoustic pressure by the absorbing ground depended on the phase angle of the complex-valued surface impedance. The results obtained using different phase angles differ more strongly with increasing magnitude of the absorption coefficient. To increase the prediction accuracy, the full impedance characteristic of the absorptive surface should be known. In cases where only the absorption coefficient is provided, the surface impedance can be assumed to be real-valued. Finally, the obtained results from simulations using different intermediate frequency steps per one-third octave band indicated that the number of intermediate steps could be reduced with decreasing bandwidth without strongly affecting the simulation results. It is also suggested to use at least three intermediate steps per frequency band to prevent larger deviations introduced by possibly occurring destructive interference in the pressure field of the single frequency. In terms of the overall sound pressure level, the finite element model using five intermediate steps per frequency band provide a prediction accuracy comparable to the initial model using nine steps while saving up almost half of the total computation time.

Future work

The developed finite element model in the framework of this thesis provides a good starting point for further research on the problem. Some examples of possible future research directions are:

- Validate the existing finite element model under real operation conditions, i.e., against pass-by measurements in the free field or in a tunnel.
- Extend the sound source modeling approach to real sound sources, especially to the wheel-rail interface, which is the main noise source of the vehicle under dynamic conditions.
- Investigate the complex surface impedance further, comparing the result with a validation measurement.

- Apply the developed finite element modeling approach to other railway vehicle types with existing validation measurements.

Bibliography

[1] Jie Zhang, Xinbiao Xiao, Xiaozhen Sheng, and Zhihui Li. Sound Source Localisation for a High-Speed Train and Its Transfer Path to Interior Noise. *Chinese Journal of Mechanical Engineering*, 32(1):59, December 2019.

[2] NoiseMeters Inc. Octave Band Filters. `https://www.noisemeters.com/help/faq/octave-filters/`. Online; accessed: 2023-01-04.

[3] Ono Sokki. What is sound level meter? `https://www.onosokki.co.jp/English/hp_e/whats_new/SV_rpt/SV_7/sv7_5.htm`. Online; accessed: 2023-01-03.

[4] Wiener Linien. Wiens neue U-Bahn: Der erste X-Wagen ist fertig! `https://www.wienerlinien.at/eportal3/ep/contentView.do/pageTypeId/66526/programId/74579/contentTypeId/1001/channelId/-48278/contentId/5001449`, 2020. Online; accessed: 2023-01-05.

[5] DIN EN ISO. 9614-2: Bestimmung der Schalleistungspegel von Geräuschquellen durch Schallintensitätsmessungen, Teil 2: Messung mit kontinuierlicher Abtastung. *Brüssel: CEN*, 1996.

[6] Andrew F. Seybert and Jun xia Han. Measurement of pavement absorption using ISO 13472-2. *Journal of the Acoustical Society of America*, 123:3686–3686, 2008.

[7] Ilona Paozalyte, Raimondas Grubliauskas, and Petras Vaitiekûnas. Research of railway noise pollution at the living area of railway station in Klaipeda City and designing of noise barrier. *Vilnius Gediminas Technical University*, January 2011.

[8] Hui Li, David Thompson, and Giacomo Squicciarini. A 2.5D acoustic finite element method applied to railway acoustics. *Applied Acoustics*, 182:108270, November 2021.

[9] R. Lundén and B. Paulsson. 1 - introduction to wheel–rail interface research. In R. Lewis and U. Olofsson, editors, *Wheel–Rail Interface Handbook*, pages 3–33. Woodhead Publishing, 2009.

[10] Hee-Min Noh. Contribution analysis of interior noise and floor vibration in high-speed trains by operational transfer path analysis. *Advances in Mechanical Engineering*, 9(8):1687814017714986, 2017.

[11] Manfred Kaltenbacher. *Numerical Simulation of Mechatronic Sensors and Actuators*. Springer, Berlin/Heidelberg, 2 edition, 2007.

[12] Manfred Kaltenbacher, editor. *Computational Acoustics*, volume 579 of *CISM International Centre for Mechanical Sciences*. Springer International Publishing, Cham, 2018.

[13] David R. Bergman. *Computational acoustics: theory and implementation*. John Wiley & Sons, Hoboken, NJ, 2018.

[14] Kurt Heutschi. Lecture Notes on Acoustics I. Lecture Notes, Swiss Federal Institute of Technology Zurich, 2016.

[15] Frank Fahy. *Foundations of engineering acoustics*. Academic, San Diego, Calif. ; London, 2001.

[16] Lawrence E. Kinsler, Austin R. Frey, Alan B. Coppens, and James V. Sanders. *Fundamentals of acoustics*. John Wiley & Sons, New York, 4 edition, January 2000.

[17] Erwin Kreyszig. *Advanced engineering mathematics; 2nd ed.* Wiley, New York, NY, 1967.

[18] C. Ray Wylie. *Advanced Engineering Mathematics*. McGraw-Hill Education, New York, NY, 6th edition, 1995.

[19] Frédéric Nataf. Absorbing boundary conditions and perfectly matched layers in wave propagation problems. In Ivan Graham, Ulrich Langer, Jens Melenk, and Mourad Sini, editors, *Direct and Inverse Problems in Wave Propagation and Applications*, pages 219–232. De Gruyter, Berlin, Boston, 2013.

[20] Bjorn Engquist and Andrew Majda. Absorbing boundary conditions for the numerical simulation of waves. *Mathematics of Computation*, 31(139):629–651, 1977.

[21] Jean-Pierre Berenger. A perfectly matched layer for the absorption of electromagnetic waves. *Journal of Computational Physics*, 114(2):185–200, 1994.

[22] Barbara Kaltenbacher, Manfred Kaltenbacher, and Imbo Sim. A modified and stable version of a perfectly matched layer technique for the 3-d second order wave equation in time domain with an application to aeroacoustics. *Journal of Computational Physics*, 235:407–422, 2013.

[23] Gh. Reza Sinambari and Stefan Sentpali. *Ingenieurakustik: Physikalische Grundlagen, Anwendungsbeispiele und Übungen*. Springer Fachmedien Wiesbaden, Wiesbaden, 2020.

[24] A.P.G. Peterson and E.E. Gross. *Handbook of Noise Measurement*. General Radio, 1972.

[25] NoiseMeters Inc. Frequency Weighting. `https://www.noisemeters.com/help/faq/frequency-weighting/`. Online; accessed: 2023-01-05.

[26] IEC 61672-1:2013(E): Electroacoustics - Sound level meters - Part 1: Specifications. Standard, International Electrotechnical Commission, Geneva, CH, September 2013.

[27] Finn Jacobsen and Hans-Elias Bree. A comparison of two different sound intensity measurement principles. *Journal of The Acoustical Society of America*, 118, 09 2005.

[28] Giovanni Moschioni, Bortolino Saggin, and Marco Tarabini. 3-d sound intensity measurements: Accuracy enhancements with virtual-instrument-based technology. *IEEE Transactions on Instrumentation and Measurement*, 57(9):1820–1829, 2008.

[29] openCFS. openCFS [Computer Software]. `https://opencfs.org/`.

[30] Comsol. Comsol software documentation. Perfectly Matched Layers (PMLs). `https://doc.comsol.com/5.5/doc/com.comsol.help.aco/aco_ug_pressure.05.106.html`. Online; accessed: 2023-01-10.

[31] QuickWave. QuickWavve software documentation. Perfectly Matched Layer (PML). `https://www.qwed.eu/QuickWave/help/general/3_3_1_perfectly_matched_layer_pml.htm`. Online; accessed: 2023-01-10.

[32] 3DS. CST Studio Suite documentation. Settings for PML Boundary. `https://space.mit.edu/RADIO/CST_online/mergedProjects/3D/special_solvopt/special_solvopt_pml_special.htm`. Online; accessed: 2023-01-10.

[33] Coreform LLC. Coreform Cubit (2022.4) [Computer Software]. `https://coreform.com/products/coreform-cubit/`.

[34] Y.L. Kuo and W.L. Cleghorn. The h-, p-, and r-refinements of finite element analysis of flexible slider crank mechanism. *Journal of Vibration and Control*, 13(4):415–435, 2007.

[35] Manfred Kaltenbacher and Sebastian Floss. Nonconforming Finite Elements Based on Nitsche-Type Mortaring for Inhomogeneous Wave Equation. *Journal of Theoretical and Computational Acoustics*, 26(03), September 2018.

[36] Tsvetan Nedkov. Modeling of 3D Impedance Tube with a Complex Termination Impedance using Finite Element Method. *Technical University Sofia*, 2015.

[37] Martin Wolkesson. Evaluation of impedance tube methods - A two microphone in-situ method for road surfaces and the three microphone transfer function method for porous materials. Master's thesis, Chalmers university of technology, 2013.

[38] Jørgen Hald, Wookeun Song, Karim Haddad, Cheol-Ho Jeong, and Antoine Richard. In-situ impedance and absorption coefficient measurements using a double-layer microphone array. *Applied Acoustics*, 143:74–83, January 2019.